

# High-order time-stable strong boundary conditions in finite-difference schemes solving hyperbolic systems

Nek Sharan<sup>a</sup>, Peter T. Brady<sup>a</sup>, and Daniel Livescu<sup>a</sup>

<sup>a</sup>*CCS-2, Los Alamos National Laboratory, Los Alamos, NM 87545, USA*

---

## Abstract

A framework to construct time-stable finite-difference schemes that apply boundary conditions strongly (or exactly) is presented for hyperbolic systems. Sufficient conditions for time-stability and conservation are derived for the linear advection equation and coupled system of hyperbolic equations using the energy method. Explicit boundary stencils and norms that satisfy those sufficient conditions are derived for global accuracies up to sixth-order. The discretization uses non-square derivative operators to allow energy and conservation conditions in terms of boundary data at grid points where physical boundary condition is applied and solution values at rest of the grid points. Diagonal-norm stencils are derived for global accuracies up to fourth-order and full-norm stencils for fourth and higher orders. In most cases, the derivation yields difference operators with multiple free parameters; a choice that avoids restrictive CFL constraints is made in those cases. Various linear and non-linear numerical tests that verify the accuracy and stability of the derived stencils are presented. Application of the proposed discretization to impose characteristic boundary conditions in fluid-flow simulations is also discussed.

*Keywords:*

High-order accuracy, time stability, boundary conditions, finite-difference methods

---

## 1. Introduction

High-fidelity fluid dynamics simulations require stable boundary closures for long-time calculations typical of practical applications. High-order centered finite-difference schemes are commonly used for accurate turbulent flow [1, 2, 3, 4] and aeroacoustics [5, 6, 7, 8] simulations because of their non-dissipative properties, ease of implementation, and computational efficiency. However, the non-dissipative character of centered schemes renders them susceptible to numerical instabilities when the boundary closure for a given interior scheme is not derived to satisfy stability conditions.

Numerical stability proofs require bounding the computational solution in terms of constants independent of grid spacing [9]. Various stability definitions exist that impose different solution bounds. The classical (Lax and G-K-S) stability definition allows non-physical solution growth in time even though the solution may converge on successive grid refinements [10, 11], which can be detrimental to long-time integrations in fluid-flow calculations. In this study, boundary stencils are, therefore, derived to satisfy the time stability (also called strict or energy stability) definition, which provides a uniform bound for the solution in time, preventing non-physical temporal growth.

Commonly used time-stable boundary treatments include the weak imposition of boundary conditions (BCs) with simultaneous-approximation-term (SAT) [11] and the projection method [12, 13]. The SAT approach imposes BCs using a penalty term, whereas the projection method uses a projection matrix to incorporate BCs into the system of ordinary differential equations (ODEs) solved for the discrete solution. The extent to which the boundary point may satisfy the BC with SAT approach depends on the magnitude

---

*Email address:* `nsharan@lanl.gov` (Nek Sharan)

of the penalty parameter. A higher value may better satisfy the BC, however, it may make the ODE system stiffer. In cases of non-homogeneous boundary data, the projection method may also not satisfy the BC exactly because the projected ODE system imposes the time-derivative of boundary data, and the time-integration of the ODE system may not be exact. This work focuses on derivation of a time-stable method that enforces BCs strongly (or exactly).

Kreiss & Scherer [14, 15] proposed a method to derive first-derivative finite-difference approximations with centered interior scheme and boundary stencils that satisfy a summation-by-parts (SBP) property of the differential equation. Their approach was employed to construct high-order SBP boundary closures for centered interior schemes of various order in [16]. In general, the SBP property is not a sufficient condition for time stability with strong BCs [9, 11], but several SBP operators are time stable for scalar hyperbolic problems with homogeneous boundary data. However, as observed by Carpenter *et al.* [11], high-order SBP operators can lead to unphysical solution growth in time for coupled hyperbolic systems, when solved using strong BCs. In particular, for the  $2 \times 2$  system discussed in [11, Section 3], and solved here in Section 4.2, Carpenter *et al.* noted at the time that no central difference scheme of order greater than two was time-stable for this system. To the best of our knowledge, there are still no central finite-difference schemes of order greater than two that are time-stable for this system with strong BCs. Carpenter *et al.* [11] proved time-stability of SBP schemes for this system with SAT (weak) BC implementation. In this work, we derive boundary stencils for centered interior schemes up to sixth-order accurate that are time-stable for this system with strong BCs.

Numerical time-stability analyses of finite-difference schemes using weak BC implementations are widely available [17, 18, 19]. However, similar analyses for strong BCs are hindered by the challenge of incorporating exact boundary conditions in the system of ODEs (following a method-of-lines approach) such that it facilitates a uniform solution bound (for systems with bounded energy), independent of grid spacing. A non-linear optimization based approach to derive time-stable boundary closures for strong BCs is proposed in [20]. In theoretical stability analyses, application of strong BCs is typically represented by a projection operator that omits rows in the derivative operator corresponding to grid points where the physical BCs are applied, e.g. [11, 15]. The row omissions prevent calculations at the boundary points where exact boundary data is injected. Row omissions in a derivative operator originally designed for calculations on the whole domain compromises the numerical properties of the full operator [9]. For example, in the conservation analysis for scalar convection equation (1), a derivative operator that ensures numerical flux cancellations across the domain, allowing only the physical boundary point contributions in the conservation condition (as desired), may not ensure such cancellations after row omission(s). To alleviate these issues, we consider non-square derivative operators that incorporate exact BCs to begin with and derive time-stability and conservation conditions for such operators. This is in contrast to the traditional approach where stability and conservation conditions are satisfied for square operators, but may not preserve those properties on row omission(s) for strong BC implementation.

The paper is organized as follows. Time-stability and conservation constraints for finite-difference schemes imposing strong BCs are derived in Section 2 for hyperbolic scalar equation as well as coupled system of equations. For non-homogeneous boundary data, a definition of strong time-stability is introduced, in addition to the time-stability definition for homogeneous boundary data. Inflow boundary stencils that incorporate strong implementation of the BC and satisfy the time-stability and conservation constraints are derived for various order of accuracies in Section 3. The proof of stability assumes a stencil with SBP property at the outflow boundary, therefore, several high-order full-norm SBP boundary closures are also derived for sixth-order centered interior schemes. The stability and accuracy of the derived schemes is evaluated for various problems in Section 4. Application of the derived schemes to solve the Euler equations with characteristic boundary conditions is discussed in Section 5.

## 2. Numerical approach and proof of stability

This section derives the constraints on boundary stencils for time-stable enforcement of strong BCs to solve a hyperbolic scalar equation (Section 2.1) and hyperbolic system of equations (Section 2.2). The derived constraints are then used to obtain schemes of various order of accuracies in Section 3.

### 2.1. The hyperbolic scalar problem

Consider the scalar hyperbolic equation

$$\frac{\partial U}{\partial t} + \frac{\partial U}{\partial x} = 0, \quad 0 \leq x \leq 1, \quad t \geq 0, \quad (1)$$

with the initial and the boundary condition given by

$$U(x, 0) = f(x), \quad U(0, t) = g(t). \quad (2)$$

On a domain with  $n + 1$  equidistant grid points  $(x_0 = 0, x_1, \dots, x_{n-1}, x_n = 1)$ , a semi-discretization of (1)–(2) using strong boundary conditions can be written as

$$\frac{d\tilde{\mathbf{u}}}{dt} = -D\mathbf{u}, \quad (3)$$

$$\mathbf{u}(0) = \mathbf{f},$$

where  $\mathbf{u}(t) = [u_0(t) \ \cdots \ u_n(t)]^T$ , with  $u_0(t) \equiv g(t)$ , is the discrete solution vector.  $\tilde{\mathbf{u}}(t) = [u_1(t) \ \cdots \ u_n(t)]^T$  is the solution vector without the first element, which corresponds to the grid point where the boundary data is injected.  $D$ , a matrix of size  $n \times (n + 1)$ , denotes the derivative operator. The entries of  $D$  are denoted by  $d_{ij}$ , where  $1 \leq i \leq n$  and  $0 \leq j \leq n$ . Its non-square structure prevents computation at the first grid point, where physical boundary condition is applied.  $\mathbf{f} = [f(x_0) \ \cdots \ f(x_n)]^T$  denotes the discrete initial data.

Define a scalar product and norm for discrete real-valued vector functions  $\mathbf{v} = [v_1 \ \cdots \ v_n]^T$  and  $\mathbf{w} = [w_1 \ \cdots \ w_n]^T$  by (e.g. [16])

$$(\mathbf{v}, \mathbf{w})_H = \mathbf{v}^T H \mathbf{w} = \sum_{i,j=1}^{\kappa} h_{ij} v_i w_j \Delta x + \sum_{i=\kappa+1}^{n-\kappa} v_i w_i \Delta x + \sum_{i,j=n-\kappa+1}^n h_{ij} v_i w_j \Delta x, \quad (4)$$

$$\|\mathbf{v}\|_H = \sqrt{(\mathbf{v}, \mathbf{v})_H}, \quad (5)$$

where  $\Delta x$  denotes the grid spacing,  $\kappa$  represents the depth of boundary stencil, and  $h_{i,j}$  are the coefficients of a symmetric positive-definite (norm) matrix  $H$ .

Multiplying (3) by  $\tilde{\mathbf{u}}^T H$ , where  $H$  is a norm matrix of size  $n \times n$ , and adding its transpose yields

$$\frac{d}{dt} \|\tilde{\mathbf{u}}\|_H^2 = -\tilde{\mathbf{u}}^T H D \mathbf{u} - (D \mathbf{u})^T H \tilde{\mathbf{u}}. \quad (6)$$

Using Definition 2.13 of [9], time-stability is defined as:

**Definition 1.** *The approximation (3) is time-stable if for  $g = 0$ , there is a unique solution  $\tilde{\mathbf{u}}(t)$  satisfying*

$$\|\tilde{\mathbf{u}}\|_H \leq K \|\tilde{\mathbf{f}}\|_H, \quad \text{or} \quad \frac{d}{dt} \|\tilde{\mathbf{u}}\|_H^2 \leq 0, \quad (7)$$

where  $K$  is independent of  $\Delta x$ ,  $\mathbf{f}$  and  $t$ .  $\tilde{\mathbf{f}}$  denotes the vector  $\mathbf{f}$  without its first element, following the definition of  $\tilde{\mathbf{u}}$ .

For  $g = 0$ , the first element of vector  $\mathbf{u}$  is zero, *i.e.*  $u_0 = 0$ . Substituting  $u_0 = 0$  in (6) yields

$$\frac{d}{dt} \|\tilde{\mathbf{u}}\|_H^2 = -\tilde{\mathbf{u}}^T H \tilde{D} \tilde{\mathbf{u}} - \left( \tilde{D} \tilde{\mathbf{u}} \right)^T H \tilde{\mathbf{u}} = \tilde{\mathbf{u}}^T \left[ H M + (H M)^T \right] \tilde{\mathbf{u}}, \quad (8)$$

where  $M = -\tilde{D}$  and  $\tilde{D}$  is a square  $(n \times n)$  matrix containing all columns of  $D$  except the first. If the approximation (3) is time-stable, *i.e.* (7) is true, then the following result about the eigenvalues of  $M$  can be stated.

**Theorem 1.** *If there exists a positive definite matrix  $H$  such that  $H M + (H M)^T$  is negative definite (semi-definite), then the real part of all eigenvalues of  $M$  are negative (non-positive).*

*Proof.* See [21, Lemma 3.1.1].  $\square$

(7) defines time-stability for homogeneous boundary data, *i.e.*  $g = 0$ . For  $g \neq 0$ , following the Definition 2.12 of [9] for strong stability, we define strong time-stability as:

**Definition 2.** *The approximation (3) is strongly time-stable if there is a unique solution  $\tilde{\mathbf{u}}(t)$  satisfying*

$$\|\tilde{\mathbf{u}}\|_H^2 \leq K \left( \|\tilde{\mathbf{f}}\|_H^2 + \int_0^t |g(\tau)|^2 d\tau \right), \quad \text{or} \quad \frac{d}{dt} \|\tilde{\mathbf{u}}\|_H^2 \leq K |g|^2, \quad (9)$$

where  $K$  is independent of  $\Delta x$ ,  $\mathbf{f}$ ,  $g$  and  $t$ .

**Remark.** The time-stability definition (7) differs from the classical stability definition [9, Definition 2.11] in requiring a uniform solution bound, independent of time [10, 11]. The energy estimates derived for the SBP operators in [15] ensure classical stability (see [15, Theorem 1.1]), but may not ensure time stability [11, 9]. The diagonal- and restricted full-norm SBP first-derivative operators of [16] on omitting their first row for strong BC implementation with semi-discretization (3) satisfy (7), for homogeneous boundary data, but do not guarantee (9) for non-zero boundary data.

In the following, we derive constraints on the entries of derivative operator,  $D$ , for the solution of (3) to satisfy (9). To simplify algebra, the non-square operator  $Q = HD$  can be decomposed such that

$$\tilde{\mathbf{u}}^T H D \mathbf{u} = \tilde{\mathbf{u}}^T Q \mathbf{u} = \tilde{\mathbf{u}}^T \tilde{Q} \tilde{\mathbf{u}} + \tilde{\mathbf{u}}^T \mathbf{q}_0 g, \quad (10)$$

where  $\tilde{Q}$  is a square  $(n \times n)$  matrix containing all columns of  $Q$  except the first and vector  $\mathbf{q}_0$  is the first column of  $Q$ .  $u_0(t) \equiv g(t)$  is substituted in the second term of r.h.s. of (10). The entries of  $Q$ , like  $D$ , are denoted by  $q_{ij}$ , where  $1 \leq i \leq n$  and  $0 \leq j \leq n$ . Substituting (10) in r.h.s. of (6) provides the strong time-stability condition that respects (9):

$$-\tilde{\mathbf{u}}^T H D \mathbf{u} - (D \mathbf{u})^T H \tilde{\mathbf{u}} = -\tilde{\mathbf{u}}^T (\tilde{Q} + \tilde{Q}^T) \tilde{\mathbf{u}} - 2\tilde{\mathbf{u}}^T \mathbf{q}_0 g \leq K |g|^2. \quad (11)$$

In addition to the above strong time-stability condition, we seek a discrete conservation condition. The quantity  $S = \int_0^1 U dx$  can be shown to depend only on boundary fluxes, since integrating (1) yields

$$\frac{dS}{dt} = - \int_0^1 \frac{\partial U}{\partial x} dx = g(t) - U(1, t). \quad (12)$$

A discrete analogue for (12) is given by

$$\frac{dS}{dt} \approx \sum_{i=1}^n \left( \frac{d}{dt} H \tilde{\mathbf{u}} \right)_i = - \sum_{i=1}^n (H D \mathbf{u})_i = g(t) - u_n(t), \quad (13)$$

where  $(\mathbf{v})_i$  denotes the  $i$ -th component of vector  $\mathbf{v} = \begin{bmatrix} v_1 & \cdots & v_n \end{bmatrix}^T$  and the entries of  $H$  constitute a quadrature for the domain  $0 \leq x \leq 1$ .

In terms of the operators defined in (10), condition (13) translates to

$$\sum_{i=1}^n (\mathbf{q}_0)_i = -1, \quad \sum_{i=1}^n q_{ij} = \begin{cases} 1 & j = n \\ 0 & \text{otherwise} \end{cases}, \quad (14)$$

where  $(\mathbf{q}_0)_i \equiv q_{i0}$ .

We seek derivative approximations,  $D$ , and norm matrices,  $H$ , that satisfy the strong time-stability condition (11) and the discrete conservation condition (13) for various orders of accuracy. The derivation proceeds by assuming an extent of non-zero elements in vector  $\mathbf{q}_0$ , denoted by  $\beta$ , *i.e.*, let

$$\mathbf{q}_0 = \begin{bmatrix} q_{10} & \cdots & q_{\beta 0} & 0 & \cdots & 0 \end{bmatrix}^T. \quad (15)$$

In other words,  $\beta > 0$  represents the depth of boundary stencils that use the physical boundary point, where the boundary data is injected, for derivative approximation. A non-zero (row) entry in  $\mathbf{q}_0$  requires a corresponding non-zero diagonal entry in  $\tilde{Q}$  to satisfy (11), as shown in the following theorem.

**Theorem 2.** (a) *The strong time-stability condition (11) is satisfied if, for  $1 \leq i, j \leq n$  and  $\beta > 0$ ,*

$$q_{ij} \begin{cases} = -q_{ji} & \text{if } i \neq j, \\ > 0 & \text{if } i = j \leq \beta, \\ \geq 0 & \text{if } i = j > \beta. \end{cases} \quad (16)$$

(b) *The conservation condition (14) is concurrently satisfied if the latter two conditions in (16), for the diagonal entries of  $\tilde{Q}$ , are replaced by stricter conditions, given by*

$$q_{ij} = \begin{cases} -q_{ji} & \text{if } i \neq j, \\ -\frac{1}{2}q_{i0} > 0 & \text{if } i = j \leq \beta, \\ 0 & \text{if } \beta < i = j < n, \\ \frac{1}{2} & \text{if } i = j = n, \end{cases} \quad (17)$$

and  $\sum_{i=1}^{\beta} q_{i0} = -1$ .

*Proof.* Matrix  $\tilde{Q}$  with entries satisfying  $q_{ij} = -q_{ji}$  for  $i \neq j$  yields

$$\frac{\tilde{Q} + \tilde{Q}^T}{2} = \text{diag}(q_{11}, \dots, q_{\beta\beta}, \dots, q_{nn}), \quad (18)$$

whose substitution in (11), with  $\mathbf{q}_0 = \begin{bmatrix} q_{10} & \cdots & q_{\beta 0} & 0 & \cdots & 0 \end{bmatrix}^T$ , provides

$$\begin{aligned} -\tilde{\mathbf{u}}^T (\tilde{Q} + \tilde{Q}^T) \tilde{\mathbf{u}} - 2\tilde{\mathbf{u}}^T \mathbf{q}_0 g &= -\sum_{i=1}^n 2q_{ii} u_i^2 - \sum_{i=1}^{\beta} 2q_{i0} u_i g \\ &= \sum_{i=1}^{\beta} \left[ -2q_{ii} \left( u_i + \frac{q_{i0}}{2q_{ii}} g \right)^2 + \frac{q_{i0}^2}{2q_{ii}} g^2 \right] - \sum_{i=\beta+1}^n 2q_{ii} u_i^2 \leq K_1 g^2, \end{aligned} \quad (19)$$

where the last inequality holds if  $q_{ii} > 0$  for  $1 \leq i \leq \beta$  and  $q_{ii} \geq 0$  for  $\beta < i \leq n$  (the conditions in (16)), and  $K_1 = \sum_{i=1}^{\beta} \frac{q_{i0}^2}{2q_{ii}}$ . This proves the (a) part of the theorem.

For the (b) part of the theorem, note first that conditions in (17) satisfy (16), which ensures strong time-stability. This can also be seen by substituting (17) in (19), and using  $\sum_{i=1}^{\beta} q_{i0} = -1$ . It remains to be shown that (17) also satisfies the conservation condition (14).

The rows of a derivative approximation,  $D$ , sum to zero and, hence, the rows of  $Q = HD$  also sum to zero (for proof, see Lemma 1 in Appendix A), *i.e.*,

$$\sum_{j=0}^n q_{ij} = q_{i0} + q_{ii} + \sum_{\substack{j=1 \\ j \neq i}}^n q_{ij} = 0 \quad \forall 1 \leq i \leq n, \quad (20)$$

where, from (15),  $q_{i0} = 0$  for  $i > \beta$ . Using  $q_{ij} = -q_{ji}$  for  $i \neq j$  (this structure is typical of centered finite-difference scheme in the interior) yields

$$\sum_{\substack{j=1 \\ j \neq i}}^n q_{ij} = - \sum_{\substack{j=1 \\ j \neq i}}^n q_{ji} \quad \forall 1 \leq i \leq n. \quad (21)$$

Adding  $-q_{ii}$  to both sides of (21) and using (20) provides

$$- \sum_{j=1}^n q_{ji} = \sum_{j=1}^n q_{ij} - 2q_{ii} = -q_{i0} - 2q_{ii} \quad \forall 1 \leq i \leq n. \quad (22)$$

(14) is then satisfied if  $q_{ii} = -\frac{1}{2}q_{i0}$  for  $1 \leq i < n$  and  $q_{ii} = \frac{1}{2} - \frac{1}{2}q_{i0}$  for  $i = n$ . From (15),  $q_{i0} = 0$  for  $i > \beta$ , which yields  $q_{ii} = \frac{1}{2}$  for  $i = n$  and  $q_{ii} = -\frac{1}{2}q_{i0} = 0$  for  $\beta < i < n$  (the conditions in (17)). This completes the proof.  $\square$

To summarize the above theorem, a skew-symmetric  $\tilde{Q}$  except at the top-left and the bottom-right corner satisfies the conservation condition (14) at the interior points and it leads to cancellations of interior point terms in (11) for time stability. The skew-symmetric structure prescribes centered derivative approximations in the interior. The top-left and the bottom-right corner of  $Q$  determine behavior at the inflow and the outflow boundary, respectively. The conditions in (17) for the outflow boundary, where no physical boundary condition is required, satisfy the summation-by-parts formula [11, 16] and, hence, SBP stencils are used at the outflow boundary in the proposed scheme. At the inflow boundary, a SBP operator with strong BCs may not guarantee (strong) time stability [9, Section 7.3]. (16) provides sufficient conditions for strong time-stability with strong BCs. Inflow boundary stencils that satisfy (16) are derived in Section 3 for various centered interior schemes.

## 2.2. The hyperbolic system

This section discusses the time-stability conditions for semi-discretization of a one-dimensional hyperbolic system using strong boundary conditions. A hyperbolic system coupled at the boundaries, considered by Carpenter *et al.* [11] and by Abarbanel & Chertock [22] to prove time-stability of finite-difference schemes with SAT (weak) BCs, is considered here with strong BCs.

The system, on domain  $0 \leq x \leq 1$  and  $t \geq 0$ , is given by

$$\frac{\partial \mathbf{U}^I}{\partial t} + \Lambda^I \frac{\partial \mathbf{U}^I}{\partial x} = 0, \quad (23)$$

$$\frac{\partial \mathbf{U}^{II}}{\partial t} + \Lambda^{II} \frac{\partial \mathbf{U}^{II}}{\partial x} = 0, \quad (24)$$

where

$$\mathbf{U}^I = \left[ U^1(x, t) \quad \cdots \quad U^k(x, t) \right]^T, \quad \Lambda^I = \text{diag}(\lambda_1, \dots, \lambda_k), \quad \text{for } \lambda_1 > \lambda_2 > \cdots > \lambda_k > 0$$

describe a system of right-moving waves and

$$\mathbf{U}^{II} = \left[ U^{k+1}(x, t) \quad \cdots \quad U^r(x, t) \right]^T, \quad \Lambda^{II} = \text{diag}(\lambda_{k+1}, \dots, \lambda_r), \quad \text{for } 0 > \lambda_{k+1} > \lambda_{k+2} > \cdots > \lambda_r,$$

describe a system of left-moving waves. The system (23)-(24) is well-posed for boundary conditions given by

$$\mathbf{U}^I(0, t) = L\mathbf{U}^{II}(0, t) + \mathbf{g}^I(t), \quad (25)$$

$$\mathbf{U}^{II}(1, t) = R\mathbf{U}^I(1, t) + \mathbf{g}^{II}(t), \quad (26)$$

where  $L$  and  $R$  are constant matrices of size  $k \times (r - k)$  and  $(r - k) \times k$ , respectively, and  $\mathbf{g}^I$  and  $\mathbf{g}^{II}$  are vectors of size  $k$  and  $r - k$ , respectively. The system (23)-(26) has a non-growing solution in time if  $\mathbf{g}^I$  and  $\mathbf{g}^{II}$  are zero and (see [11, Theorem 2.1])

$$\|L\| \|R\| \leq 1. \quad (27)$$

The matrix norm for real matrices is defined by  $\|L\|^2 = \rho(L^T L)$ , where  $\rho(\cdot)$  denotes the spectral radius.

A semi-discretization of (23)-(26) using strong boundary conditions can be written as

$$\frac{d\mathbf{w}}{dt} = -\mathcal{D}\mathbf{w}, \quad (28)$$

where  $\mathbf{w}(t) = \begin{bmatrix} \tilde{\mathbf{u}}^I(t) & \tilde{\mathbf{u}}^{II}(t) \end{bmatrix}^T$  with  $\tilde{\mathbf{u}}^I(t) = \begin{bmatrix} \tilde{\mathbf{u}}^1(t) & \cdots & \tilde{\mathbf{u}}^k(t) \end{bmatrix}$  and  $\tilde{\mathbf{u}}^{II}(t) = \begin{bmatrix} \tilde{\mathbf{u}}^{k+1}(t) & \cdots & \tilde{\mathbf{u}}^r(t) \end{bmatrix}$ . The unknowns for each equation in the system are given, assuming a discretization with  $n + 1$  grid points, as described in Section 2.1, by  $\tilde{\mathbf{u}}^\phi(t) = \begin{bmatrix} u_1^\phi(t) & \cdots & u_n^\phi(t) \end{bmatrix}^T$  for  $1 \leq \phi \leq k$  and by  $\tilde{\mathbf{u}}^\phi(t) = \begin{bmatrix} u_0^\phi(t) & \cdots & u_{n-1}^\phi(t) \end{bmatrix}^T$  for  $k + 1 \leq \phi \leq r$ , where  $\tilde{\mathbf{u}}^\phi(t)$  is the solution vector without the element corresponding to the grid point where boundary data is injected. Therefore, the solution vectors for the first  $k$  equations do not contain the element corresponding to the first grid point and the rest do not contain the element corresponding to the last grid point.

The derivative operator,  $\mathcal{D}$ , is then given by

$$\mathcal{D} = \Lambda \mathcal{H}^{-1} \mathcal{Q}, \quad (29)$$

where  $\Lambda = \text{diag}(\lambda_1, \dots, \lambda_r)$ ,

$$\mathcal{H} = \begin{bmatrix} \mathcal{H}_{11} & 0 \\ 0 & \mathcal{H}_{22} \end{bmatrix}, \quad \text{and} \quad \mathcal{Q} = \begin{bmatrix} \mathcal{Q}_{11} & \mathcal{Q}_{12} \\ \mathcal{Q}_{21} & \mathcal{Q}_{22} \end{bmatrix}.$$

The submatrices are given by

$$\begin{aligned} \mathcal{H}_{11} &= I_k \otimes H, & \mathcal{H}_{22} &= I_{r-k} \otimes H^\#, \\ \mathcal{Q}_{11} &= I_k \otimes \tilde{Q}, & \mathcal{Q}_{12} &= L \otimes Q_0, & \mathcal{Q}_{21} &= -R \otimes Q_0^\#, & \mathcal{Q}_{22} &= -I_{r-k} \otimes \tilde{Q}^\#, \end{aligned} \quad (30)$$

where  $I_m$  denotes an identity matrix of size  $m \times m$  and  $\otimes$  denotes the Kronecker product. The superscript  $\#$  denotes the matrix and vector transformations  $M^\# = \mathcal{J}^{-1} M \mathcal{J}$  and  $\mathbf{m}^\# = \mathcal{J}^{-1} \mathbf{m}$ , respectively, where

$$\mathcal{J} = \mathcal{J}^{-1} = \begin{bmatrix} 0 & & 1 \\ & \ddots & \\ 1 & & 0 \end{bmatrix}. \quad (31)$$

The transformation yields matrix/vector “rotated” by  $180^\circ$ , for example,

$$\begin{bmatrix} a & b \\ c & d \end{bmatrix}^\# = \begin{bmatrix} d & c \\ b & a \end{bmatrix} \quad \text{and} \quad \begin{bmatrix} a \\ b \end{bmatrix}^\# = \begin{bmatrix} b \\ a \end{bmatrix}. \quad (32)$$

$Q_0$  is a  $n \times n$  matrix with  $\mathbf{q}_0$  as the first column and remaining columns zero. The vector  $\mathbf{q}_0$  and matrices  $H$  and  $\tilde{Q}$  are as described in Section 2.1.

Let the discrete energy be defined as (e.g., [11, 22])

$$E(t) = \sum_{\phi=1}^k \frac{\|R\|}{\lambda_\phi} (\tilde{\mathbf{u}}^\phi)^T H \tilde{\mathbf{u}}^\phi + \sum_{\phi=k+1}^r \frac{\|L\|}{|\lambda_\phi|} (\tilde{\mathbf{u}}^\phi)^T H^\# \tilde{\mathbf{u}}^\phi,$$

which provides the time-stability condition:

$$\frac{dE}{dt} = \sum_{\phi=1}^k \frac{\|R\|}{\lambda_{\phi}} \frac{d}{dt} (\tilde{\mathbf{u}}^{\phi})^T H \tilde{\mathbf{u}}^{\phi} + \sum_{\phi=k+1}^r \frac{\|L\|}{|\lambda_{\phi}|} \frac{d}{dt} (\tilde{\mathbf{u}}^{\phi})^T H^{\#} \tilde{\mathbf{u}}^{\phi} \leq 0. \quad (33)$$

The conservation condition for the system (23)-(24) is same as that for the scalar equation (1), since the system is comprised of scalar advection equations. The conservation condition for the operators used in semi-discretization (28) is, therefore, given by (14). The numerical flux should “telescope” across a domain to the boundaries without loss, consistent with the continuous flux behavior.

The following theorem provides sufficient conditions for the semi-discretization (28) to satisfy the time-stability and conservation conditions.

**Theorem 3.** (a) *The time-stability condition (33) is satisfied if, for  $1 \leq i, j \leq n$  and  $\beta > 0$ ,*

$$q_{ij} \begin{cases} = -q_{ji} & \text{if } i \neq j, \\ \geq \frac{q_{i0}^2}{4q_{nn}a_i} \|L\| \|R\| & \text{if } i = j \leq \beta, \\ \geq 0 & \text{if } \beta < i = j < n, \\ > 0 & \text{if } i = j = n, \end{cases} \quad (34)$$

where  $a_i > 0$  and  $\sum_{i=1}^{\beta} a_i = 1$ .

(b) *The conservation condition (14) is concurrently satisfied if (17) is true with  $\sum_{i=1}^{\beta} q_{i0} = -1$ .*

*Proof.* The individual terms in summations of (33), that denote the contribution from each equation of the system, are given by

$$\frac{d}{dt} (\tilde{\mathbf{u}}^{\phi})^T H \tilde{\mathbf{u}}^{\phi} = \frac{d}{dt} \|\tilde{\mathbf{u}}^{\phi}\|_H^2 = -\lambda_{\phi} (\tilde{\mathbf{u}}^{\phi})^T (\tilde{Q} + \tilde{Q}^T) \tilde{\mathbf{u}}^{\phi} - 2\lambda_{\phi} (\tilde{\mathbf{u}}^{\phi})^T \mathbf{q}_0 (L\tilde{\mathbf{u}}_0^{II})_{\phi}, \quad 1 \leq \phi \leq k, \quad (35)$$

$$\frac{d}{dt} (\tilde{\mathbf{u}}^{\phi})^T H^{\#} \tilde{\mathbf{u}}^{\phi} = \frac{d}{dt} \|\tilde{\mathbf{u}}^{\phi}\|_{H^{\#}}^2 = -\lambda_{\phi} (\tilde{\mathbf{u}}^{\phi})^T (\tilde{Q}^{\#} + (\tilde{Q}^{\#})^T) \tilde{\mathbf{u}}^{\phi} - 2\lambda_{\phi} (\tilde{\mathbf{u}}^{\phi})^T \mathbf{q}_0^{\#} (R\tilde{\mathbf{u}}_n^I)_{\phi}, \quad k+1 \leq \phi \leq r, \quad (36)$$

where  $\tilde{\mathbf{u}}_0^{II} = [u_0^{k+1}(t) \ u_0^{k+2}(t) \ \cdots \ u_0^r(t)]^T$  and  $\tilde{\mathbf{u}}_n^I = [u_n^1(t) \ u_n^2(t) \ \cdots \ u_n^k(t)]^T$ . Assuming  $q_{ij} = -q_{ji}$ , for  $i \neq j$  in matrix  $\tilde{Q}$ , the contribution to (33) from the first term in the r.h.s. of (35) and (36) can be calculated from, respectively,

$$\sum_{\phi=1}^k (\tilde{\mathbf{u}}^{\phi})^T (\tilde{Q} + \tilde{Q}^T) \tilde{\mathbf{u}}^{\phi} = 2 \sum_{i=1}^n q_{ii} \sum_{\phi=1}^k (u_i^{\phi})^2 = 2 \sum_{i=1}^n q_{ii} \|\tilde{\mathbf{u}}_i^I\|^2, \quad (37)$$

$$\sum_{\phi=k+1}^r (\tilde{\mathbf{u}}^{\phi})^T (\tilde{Q}^{\#} + (\tilde{Q}^{\#})^T) \tilde{\mathbf{u}}^{\phi} = -2 \sum_{i=1}^n q_{ii} \sum_{\phi=k+1}^r (u_{n-i}^{\phi})^2 = -2 \sum_{i=1}^n q_{ii} \|\tilde{\mathbf{u}}_{n-i}^{II}\|^2, \quad (38)$$

where  $\|\tilde{\mathbf{u}}_i^I\|^2 = \sum_{\phi=1}^k (u_i^{\phi})^2$  and  $\|\tilde{\mathbf{u}}_{n-i}^{II}\|^2 = \sum_{\phi=k+1}^r (u_{n-i}^{\phi})^2$ . Further, assuming  $\mathbf{q}_0 = [q_{10} \ \cdots \ q_{\beta 0} \ 0 \ \cdots \ 0]^T$ , the contribution to (33) from the second term in the r.h.s. of (35) and (36) are, respectively,

$$\sum_{\phi=1}^k (\tilde{\mathbf{u}}^{\phi})^T \mathbf{q}_0 (L\tilde{\mathbf{u}}_0^{II})_{\phi} = \sum_{i=1}^{\beta} q_{i0} \sum_{\phi=1}^k u_i^{\phi} (L\tilde{\mathbf{u}}_0^{II})_{\phi}, \quad (39)$$

$$\sum_{\phi=k+1}^r (\tilde{\mathbf{u}}^{\phi})^T \mathbf{q}_0^{\#} (R\tilde{\mathbf{u}}_n^I)_{\phi} = - \sum_{i=1}^{\beta} q_{i0} \sum_{\phi=k+1}^r u_{n-i}^{\phi} (R\tilde{\mathbf{u}}_n^I)_{\phi}. \quad (40)$$



Using the Cauchy-Schwarz inequality

$$\sum_{\phi=1}^k u_i^\phi (L\tilde{\mathbf{u}}_0^{II})_\phi \leq \|\tilde{\mathbf{u}}_i^I\| \|L\| \|\tilde{\mathbf{u}}_0^{II}\| \quad \text{and} \quad \sum_{\phi=k+1}^r u_{n-i}^\phi (R\tilde{\mathbf{u}}_n^I)_\phi \leq \|\tilde{\mathbf{u}}_{n-i}^{II}\| \|R\| \|\tilde{\mathbf{u}}_n^I\|. \quad (41)$$

Substituting (41) in (39) and (40), respectively, and, in turn, using (35)-(36) with (37)-(40) in (33), assuming  $q_{ii} \geq 0$  for  $\beta < i < n$ , it can be shown

$$\begin{aligned} \frac{dE}{dt} \leq & \left\{ \sum_{i=1}^{\beta} \left( -2q_{ii} \|R\| \|\tilde{\mathbf{u}}_i^I\|^2 + 2|q_{i0}| \|L\| \|R\| \|\tilde{\mathbf{u}}_i^I\| \|\tilde{\mathbf{u}}_0^{II}\| \right) - 2q_{nn} \|L\| \|\tilde{\mathbf{u}}_0^{II}\|^2 \right\} \\ & + \left\{ \sum_{i=1}^{\beta} \left( -2q_{ii} \|L\| \|\tilde{\mathbf{u}}_{n-i}^{II}\|^2 + 2|q_{i0}| \|L\| \|R\| \|\tilde{\mathbf{u}}_n^I\| \|\tilde{\mathbf{u}}_{n-i}^{II}\| \right) - 2q_{nn} \|R\| \|\tilde{\mathbf{u}}_n^I\|^2 \right\}. \end{aligned} \quad (42)$$

The time-stability condition (33) is satisfied if both curly brackets in (42) are non-positive. Introducing  $\sum_{i=1}^{\beta} a_i = 1$ , where  $a_i > 0$ , the last term in the curly brackets can be written as

$$2q_{nn} \|L\| \|\tilde{\mathbf{u}}_0^{II}\|^2 = 2 \sum_{i=1}^{\beta} a_i q_{nn} \|L\| \|\tilde{\mathbf{u}}_0^{II}\|^2 \quad \text{and} \quad 2q_{nn} \|R\| \|\tilde{\mathbf{u}}_n^I\|^2 = 2 \sum_{i=1}^{\beta} a_i q_{nn} \|R\| \|\tilde{\mathbf{u}}_n^I\|^2. \quad (43)$$

Substituting (43) in (42),  $dE/dt \leq 0$  if

$$q_{ii} \geq \frac{q_{i0}^2}{4q_{nn}a_i} \|L\| \|R\|, \quad 1 \leq i \leq \beta. \quad (44)$$

This proves the (a) part of the theorem.

Theorem 2(b) shows that (17) with  $\sum_{i=1}^{\beta} q_{i0} = -1$ , where  $q_{i0} \leq 0$ , satisfies the discrete conservation condition (14) for the scalar advection equation. As already mentioned, the discrete conservation condition for the system (23)-(24) is the same as that for the scalar advection equation. Therefore, a stencil satisfying (17) provides a conservative scheme for the system (23)-(24). It remains to be shown that (17) also satisfies the time-stability condition (33).

Using  $a_i = -q_{i0}$ , (17) automatically satisfies (34) since

$$-\frac{1}{2}q_{i0} = \frac{q_{i0}^2}{4q_{nn}a_i} \geq \frac{q_{i0}^2}{4q_{nn}a_i} \|L\| \|R\| \quad (45)$$

for  $\|L\| \|R\| \leq 1$ . Note that  $q_{nn} = \frac{1}{2}$  in (17). This completes the proof.  $\square$

Stencil derivation for various orders of accuracy is discussed in the next section. The goal is to satisfy the stability and conservation conditions of Theorems 2 and 3, which follows if a stencil satisfies (17) with  $\sum_{i=1}^{\beta} q_{i0} = -1$ . However, as observed in the next section, for global orders of accuracy higher than second, stencils that satisfy (17) were not found. Therefore, for third and higher global orders, stencils that satisfy (34) are derived, which also ensures (16) is satisfied, providing a time-stable scheme for the scalar problem (1)-(2) as well as for the hyperbolic system (23)-(27). The time-stability condition (34), however, does not ensure that the conservation condition (13) is satisfied.

The condition (13) with an  $\mathcal{O}(\Delta x)$  error, given by

$$\frac{dS}{dt} \approx \sum_{i=1}^n \left( \frac{d}{dt} H\tilde{\mathbf{u}} \right)_i = - \sum_{i=1}^n (HD\mathbf{u})_i = g(t) - u_n(t) + \mathcal{O}(\Delta x), \quad (46)$$

can be satisfied, concurrently with (34), if

$$q_{ij} \begin{cases} = -q_{ji} & \text{if } i \neq j, \\ \geq \frac{q_{i0}^2}{4q_{nn}a_i} \|L\| \|R\| & \text{if } i = j \leq \beta, \\ = 0 & \text{if } \beta < i = j < n, \\ = \frac{1}{2} & \text{if } i = j = n, \end{cases} \quad (47)$$

and  $\sum_{j=0}^{\beta} \sum_{i=1}^{\kappa} q_{ij} = -1$ , where  $a_i$  is as in Theorem 3 and  $\kappa$  is the depth of the boundary block in  $\tilde{Q}$  (as described in Section 3.2). Obviously, condition (46) converges to (13) as  $\Delta x \rightarrow 0$ .

For brevity, the above-derived conditions will be referred in the following sections as:

- Condition I: if a stencil satisfies (17) with  $\sum_{i=1}^{\beta} q_{i0} = -1$ ,
- Condition II: if a stencil satisfies (47) with  $\sum_{j=0}^{\beta} \sum_{i=1}^{\kappa} q_{ij} = -1$ .

Both conditions ensure time-stability for the scalar problem (1)-(2) as well as for the hyperbolic system (23)-(27). But while Condition I directly satisfies the conservation condition (13), Condition II satisfies the conservation condition to within an  $\mathcal{O}(\Delta x)$  error, given by (46).

**Remark.** To put the  $\mathcal{O}(\Delta x)$  error in context, the commonly-used approach of strong BC implementation [9, 15], using a projection operator that omits rows (corresponding to the grid points where the boundary data is injected) in a square derivative operator, introduces an  $\mathcal{O}(1)$  conservation error, as shown in Lemma 2 of Appendix A for the scalar problem (1), for example.

### 3. Stencils for various order of accuracies

The stability conditions derived in Sections 2.1 and 2.2 assume a real symmetric positive-definite matrix  $H$ . If the matrix  $H$  is diagonal, the corresponding stencil is referred to as a diagonal-norm stencil and if  $H$  has a block structure at the boundaries, the stencil is referred to as a full-norm stencil, following the nomenclature used in [16].

The derived schemes are denoted by  $p_b - p_i - p_b$ , where  $p_b$  and  $p_i$  are the order-of-accuracy of boundary and interior stencils, respectively. If an energy estimate exists, the global order-of-accuracy of a  $p_b - p_i - p_b$  scheme, where  $p_b < p_i$ , is expected to be  $p_b + 1$  for first-order hyperbolic systems [23, 24]. The structure of the operators  $H$ ,  $D$  and  $Q$  discussed below are as described in the previous section. The outflow boundary, which corresponds to the bottom-right corner of the operators, uses SBP stencils. New stencils are derived for the inflow boundary, the top-left corner of the operators. Centered schemes are used in the interior. IPOPT [25] is used to solve the non-linear optimization problems encountered in the following derivations.

#### 3.1. 1 - 2 - 1 scheme

Assume  $\beta = 1$ , i.e. let  $\mathbf{q}_0 = [q_{10} \ 0 \ \cdots \ 0]^T$ ,  $H = \Delta x \text{diag}(h_{11}, 1, \cdots, 1, \frac{1}{2})$ , and  $\tilde{Q}$  of the form

$$\tilde{Q} = \begin{bmatrix} q_{11} & \frac{1}{2} & & & \\ -\frac{1}{2} & 0 & \frac{1}{2} & & \\ & -\frac{1}{2} & 0 & \frac{1}{2} & \\ & & \ddots & \ddots & \ddots \\ & & & -\frac{1}{2} & 0 & \frac{1}{2} \\ & & & & -\frac{1}{2} & \frac{1}{2} \end{bmatrix}. \quad (48)$$

Applying first-order accuracy constraints at the boundary yields

$$q_{10} = \frac{1}{2} - h_{11}, \quad q_{11} = -1 + h_{11}.$$

$h_{11} > 1$  provides parameters that satisfy (16).  $h_{11} = \frac{3}{2}$  provides parameters that satisfy Condition I, yielding a time-stable and conservative scheme for the scalar problem and the system. Derivative approximation and the norm matrix are then given by

$$D = \frac{1}{\Delta x} \begin{bmatrix} -\frac{2}{3} & \frac{1}{3} & \frac{1}{3} & & \\ & -\frac{1}{2} & 0 & \frac{1}{2} & \\ & & \ddots & \ddots & \ddots \\ & & & -\frac{1}{2} & 0 & \frac{1}{2} \\ & & & & -1 & 1 \end{bmatrix}, \quad H = \Delta x \begin{bmatrix} \frac{3}{2} & & & & \\ & 1 & & & \\ & & \ddots & & \\ & & & 1 & \\ & & & & \frac{1}{2} \end{bmatrix}. \quad (49)$$

### 3.2. 2 – 4 – 2 scheme

Assume  $\tilde{Q}$  with an upper left unknown boundary block of size  $\kappa \times \kappa$ ,  $q_{ij} = -q_{ji}$  for  $i \neq j$  and fourth-order centered stencils in the interior, given by

$$\tilde{Q} = \begin{bmatrix} q_{11} & \cdots & q_{1\kappa-1} & q_{1\kappa} & & & \\ \vdots & \ddots & \vdots & \vdots & & & \\ -q_{1\kappa-1} & \cdots & q_{\kappa-1\kappa-1} & q_{\kappa-1\kappa} & -\frac{1}{12} & & \\ -q_{1\kappa} & \cdots & -q_{\kappa-1\kappa} & q_{\kappa\kappa} & \frac{2}{3} & -\frac{1}{12} & \\ & & \frac{1}{12} & -\frac{2}{3} & 0 & \frac{2}{3} & -\frac{1}{12} \\ & & & \ddots & \ddots & \ddots & \ddots \end{bmatrix}, \quad (50)$$

and

$$H = \Delta x \text{diag} (h_{11}, \dots, h_{\kappa-1\kappa-1}, h_{\kappa\kappa}, 1, \dots). \quad (51)$$

If an energy estimate exists, global third-order accuracy is expected with second-order accuracy at boundary points when the interior stencils are fourth-order accurate [23, 24].

To begin derivation, a value of  $\beta = 1$  and  $\kappa = 2$  is considered to determine second-order accurate boundary stencil. Remaining free parameters, after satisfying the order-of-accuracy constraints, are chosen to satisfy Condition I or II. If the number of free parameters are insufficient to satisfy either of those conditions,  $\beta$  and  $\kappa$  are systematically incremented to allow for more free parameters.

No stencil that satisfied Condition I was found for values of  $\beta$  and  $\kappa$  up to 6, and contradictory constraints arising in all cases indicate that further increase in values of  $\beta$  and  $\kappa$  may not help. Moreover, it is preferable to keep the boundary block size to a minimum to minimize bandwidth, for computational efficiency, as well as to minimize error by reducing the number of points computed at accuracies lower than the interior points.

Appendix B.1 provides a stencil using  $\beta = 4$  and  $\kappa = 4$  that satisfies Condition II for  $\|L\| \|R\| \leq 1/4$ . At the outflow boundary, second-order accurate SBP diagonal-norm boundary stencil is used [16, Appendix A]. Condition I or II offers sufficient conditions for time-stability, but not the necessary conditions. Therefore, although Condition II is satisfied by the stencil in Appendix B.1 for  $\|L\| \|R\| \leq 1/4$ , numerical eigenvalue analyses show that the stencil provides time-stable solution even when  $1/4 < \|L\| \|R\| \leq 1$ , as demonstrated in Section 4.2, for example. Similar extension of the time-stability properties of a stencil beyond the  $\|L\| \|R\|$  values for which the sufficient conditions are provably satisfied was also observed in [26].

Stencils that satisfy Condition II for smaller  $\|L\| \|R\|$  values were also found for  $\beta = 2$  and 3. However, none of those stencils were time-stable for the  $\|L\| \|R\| = 1$  system of Section 4.2, and they are not quoted here. The Appendix B.1 stencil is obtained by a non-linear optimization that maximizes  $\|L\| \|R\|$ , while satisfying Condition II. Several stencils are obtained from the optimization by changing the range of free-parameter values; one that ensures time-stable solution for  $\|L\| \|R\| \leq 1$  systems (checked by eigenvalue analysis), without imposing restrictive CFL constraints in time integration, is quoted in Appendix B.1.

### 3.3. 3 – 4 – 3 scheme

If an energy estimate exists, global fourth-order accuracy is expected from third-order accurate boundary and fourth-order accurate interior stencils [23, 24]. Assuming a  $\tilde{Q}$  and a diagonal  $H$  matrix of the form (50) and (51), respectively, does not yield boundary stencils that satisfy even the order-of-accuracy constraints for values of  $\beta$  and  $\kappa$  up to 6. Therefore, a full norm of the form (B.2) is considered, and Appendix B.2 provides operators, using  $\beta = \kappa = 4$ , that satisfy Condition II for  $\|L\| \|R\| \leq 1/6$ , obtained from the optimization procedure described in Section 3.2. At the outflow boundary, SBP full-norm stencil of third-order accuracy is used [16, Appendix B]; the free-parameter values of  $x_1 = 205.21989519227265$  and  $x_2 = 2339.702706210616$  are chosen that minimize the spectral radius to avoid restrictive time-step constraint. The stencils in Appendix B.2 satisfy Condition II for  $\|L\| \|R\| \leq 1/6$ , however, numerical results show time-stability also when  $1/6 < \|L\| \|R\| \leq 1$ , as demonstrated in Section 4.2.

No time-stable stencil for the  $\|L\| \|R\| = 1$  system of Section 4.2 was found for values of  $\beta, \kappa < 4$ , and attempts to find a stencil that satisfies Condition I were also unsuccessful.

### 3.4. 3 – 6 – 3 scheme

Assume  $\tilde{Q}$  with a  $\kappa \times \kappa$  unknown boundary block and sixth-order centered interior stencils, given by

$$\tilde{Q} = \begin{bmatrix} q_{11} & \cdots & q_{1\kappa-2} & q_{1\kappa-1} & q_{1\kappa} & & & & & \\ \vdots & \ddots & \vdots & \vdots & \vdots & & & & & \\ -q_{1\kappa-2} & \cdots & q_{\kappa-2\kappa-2} & q_{\kappa-2\kappa-1} & q_{\kappa-2\kappa} & \frac{1}{60} & & & & \\ -q_{1\kappa-1} & \cdots & -q_{\kappa-2\kappa-1} & q_{\kappa-1\kappa-1} & q_{\kappa-1\kappa} & -\frac{3}{20} & \frac{1}{60} & & & \\ -q_{1\kappa} & \cdots & -q_{\kappa-2\kappa} & -q_{\kappa-1\kappa} & q_{\kappa\kappa} & \frac{3}{4} & -\frac{3}{20} & \frac{1}{60} & & \\ & & -\frac{1}{60} & \frac{3}{20} & -\frac{3}{4} & 0 & \frac{3}{4} & -\frac{3}{20} & \frac{1}{60} & \\ & & & \ddots & \ddots & \ddots & \ddots & \ddots & \ddots & \ddots \end{bmatrix}, \quad (52)$$

and a diagonal  $H$  given by (51). The derivation follows a similar procedure as Section 3.2. The free parameters, left after satisfying the order-of-accuracy constraints, are determined to satisfy Condition I or II.

As with 3 – 4 – 3 scheme, contradictory constraints arise in attempts to satisfy Condition I for values of  $\beta$  and  $\kappa$  up to 9. Therefore, stencils that satisfy Condition II are sought. Several stencils that satisfy Condition II for values of  $\|L\| \|R\| \leq 1/12$  were found from the optimization procedure described in Section 3.2. However, none of those stencils are time-stable for  $\|L\| \|R\| = 1$  systems.

Diagonal-norm stencils have a favorable property that the theoretical stability results derived on a uniform Cartesian grid extend to curvilinear grids [27]. Therefore, despite not being time-stable for  $\|L\| \|R\| = 1$  systems, a diagonal-norm stencil, using  $\beta = \kappa = 6$ , that satisfy Condition II for  $\|L\| \|R\| \leq 1/12$  is provided in Appendix B.3.1, labeled 3 – 6 – 3 (A). At the outflow boundary, third-order accurate diagonal-norm SBP boundary stencil of [16, Appendix A] is used. Stability of this diagonal-norm stencil for various problems is discussed in Sections 4 and 5.

To derive a time-stable 3 – 6 – 3 scheme for  $\|L\| \|R\| \leq 1$  systems, a full norm of the form (B.2) is considered, and Appendix B.3.2 provides a stencil, labeled 3 – 6 – 3 (B), using  $\beta = \kappa = 4$ , that satisfies Condition II for  $\|L\| \|R\| \leq 1/3$ . Numerical eigenvalue analyses show that the stencil is also time-stable for  $1/3 < \|L\| \|R\| \leq 1$  systems, including the  $\|L\| \|R\| = 1$  system of Section 4.2. The outflow boundary uses a third-order full-norm SBP boundary stencil for sixth-order centered interior scheme, reported here for the first time. This SBP stencil is not unique, and uses free parameter values that minimize the spectral radius of the derivative operator.

### 3.5. 4 – 6 – 4 scheme

Global accuracy can be improved by increasing the accuracy of boundary stencils to fourth order. A  $\tilde{Q}$  and a diagonal  $H$  matrix of the form (52) and (51), respectively, do not yield boundary stencils that satisfy even the order-of-accuracy constraints for values of  $\beta$  and  $\kappa$  up to 9. Therefore, a full norm of the form (B.2) is considered, and Appendix B.4.1 provides a stencil, labeled 4 – 6 – 4 (A), derived using  $\beta = \kappa = 5$  and the optimization procedure described in Section 3.2, that satisfies Condition II for  $\|L\| \|R\| \leq 1/6$ . The outflow boundary uses a fourth-order full-norm SBP boundary stencil for sixth-order centered interior scheme, given in Appendix B.4, reported here for the first time. The SBP stencil is not unique, and the free parameters are chosen to minimize the spectral radius of the derivative operator.

The stencil in Appendix B.4.1 with the SBP stencil of Appendix B.4 at outflow boundary is time-stable for the scalar hyperbolic problem (1)–(2), but not for the  $\|L\| \|R\| = 1$  coupled systems. In fact, no stencil obtained from the optimization aimed at maximizing  $\|L\| \|R\|$ , while satisfying all constraints of Condition II, was found to be time-stable for  $\|L\| \|R\| = 1$  systems. Relaxing an inequality constraint of (47) in solving the non-linear optimization problem, however, yields several time-stable stencils for  $\|L\| \|R\| \leq 1$  systems. One such stencil that avoids restrictive CFL constraint is provided in Appendix B.4.2, labeled 4 – 6 – 4 (B), where the outflow boundary uses the SBP stencil of Appendix B.4. As mentioned before, Condition I or II provide sufficient conditions for time-stability, but not the necessary conditions. Therefore, all stencils that yield time-stable solutions need not necessarily satisfy Condition I or II, as also demonstrated by the derivations in [20].

Stability of the two 4 – 6 – 4 stencils will be further analyzed in Sections 4 and 5.

### 3.6. 5 – 6 – 5 scheme

If an energy estimate exists, fifth-order accurate boundary stencils with sixth-order interior scheme can provide a global sixth-order scheme [23, 24]. As in the case of 4 – 6 – 4 scheme, no diagonal-norm stencil using  $\tilde{Q}$  and  $H$  of the form (52) and (51), respectively, that satisfy the order-of-accuracy constraints was found for values of  $\beta$  and  $\kappa$  up to 10. Appendix B.5.1 provides a stencil, labeled 5 – 6 – 5 (A), derived using a full norm of the form (B.2) and  $\beta = \kappa = 6$  that satisfies Condition II for  $\|L\| \|R\| \leq 1/18$ , obtained from the optimization procedure described in Section 3.2. The outflow boundary uses the fifth-order full-norm SBP boundary stencil of Appendix B.5, derived here for the first time. The SBP stencil is not unique, and the free parameters are chosen to minimize the spectral radius of the derivative operator.

The 5 – 6 – 5 (A) stencil is time-stable for the scalar hyperbolic problem (1)–(2), but not for the  $\|L\| \|R\| = 1$  systems and, therefore, another 5 – 6 – 5 stencil is included in Appendix B.5.2, labeled 5 – 6 – 5 (B), derived by relaxing an inequality constraint in Condition II. The 5 – 6 – 5 (B) scheme has superior stability properties than the 5 – 6 – 5 (A) scheme, as shown in Sections 4 and 5. However, the (A) stencil is still included because it satisfies the sufficient conditions of stability (Condition II) for small  $\|L\| \|R\|$  values which make it provably time-stable for decoupled systems. Appendix B.4.2 and Appendix B.5.2 emphasize that the derived stability conditions of Section 2 are sufficient conditions but not necessary.

To summarize this section, boundary stencils that may provide schemes with global order-of-accuracy up to sixth-order for strong BC implementation are derived. The 1 – 2 – 1 scheme (49) satisfies Condition I. The schemes higher than second-order, provided in Appendix B, satisfy Condition II for different  $\|L\| \|R\|$  values, except the 4 – 6 – 4 (B) and 5 – 6 – 5 (B) stencils in Appendix B.4.2 and Appendix B.5.2, respectively, that are obtained by relaxing some Condition II constraints. Two stencils each for the 3 – 6 – 3, 4 – 6 – 4 and 5 – 6 – 5 schemes are provided, labeled by suffixes (A) and (B). The (A) stencils have some useful theoretical properties, for example, 3 – 6 – 3 (A) is a diagonal-norm stencil and all (A) stencils satisfy Condition II, although for small  $\|L\| \|R\|$  values. The (B) schemes, however, show better stability properties, as discussed in the following sections.

## 4. Numerical results

This section examines numerical results from application of the schemes derived in the previous section. In all cases, time integration is performed using the classical fourth-order Runge-Kutta (RK4) method with a CFL of 0.8, unless mentioned otherwise. For convergence studies, the time step is taken small enough such that the temporal errors are insignificant compared to the spatial truncation errors. The schemes derived in Section 3 allow imposition of exact boundary conditions (EBC), therefore, for brevity, we will refer to them as EBC schemes in the following sections.

### 4.1. 1-D scalar advection equation

Consider the scalar hyperbolic equation (1) with initial and boundary conditions given by

$$u(x, 0) = \sin 2\pi x, \quad u(0, t) = g(t) = \sin 2\pi(-t). \quad (53)$$

The exact solution to the problem is  $u(x, t) = \sin 2\pi(x - t)$ . A semi-discretization to the problem, using strong BCs, the notation of (3), and the decomposition described in (10), is given by

$$\frac{d\tilde{\mathbf{u}}}{dt} = -D\mathbf{u} = -H^{-1}\tilde{Q}\tilde{\mathbf{u}} - H^{-1}\mathbf{q}_0g. \quad (54)$$

For a bounded boundary data  $g(t)$ , the stability of the semi-discretization depends on the properties of the matrix  $M = -H^{-1}\tilde{Q}$ , referred to as the system matrix [28]. If the semi-discretization (54) is time-stable (as per Definition 1), then, from Theorem 1, the real part of all eigenvalues of the system matrix,  $M$ , must be non-positive. Figure 1 shows the eigenvalue spectrum of the system matrix using the EBC schemes with arbitrarily chosen number of grid points  $n = 40, 73$ , and  $108$ . All eigenvalues for all schemes lie in strict left half of the complex plane and, therefore, all the schemes show time-stability for this problem.

Table 1 shows the  $L_2$ - and  $L_\infty$ -norm of the solution error, denoted by  $\varepsilon$ , and the respective convergence rates from the EBC schemes. As expected, all schemes converge with at least  $p_b + 1$  global order-of-accuracy, where  $p_b$  is the order-of-accuracy of boundary stencils, except the  $4-6-4$  schemes that exhibit an accuracy between 4 and 5. Error at individual grid points in the  $5-6-5$  (B) simulation approaches machine precision at resolutions finer than  $n = 320$ , therefore, values for  $n = 640$  are not included for that scheme.

### 4.2. 1-D coupled hyperbolic system

This section examines the performance of the EBC schemes for a  $2 \times 2$  system coupled by the boundary conditions. This system provides a severe test of numerical stability [11, 22], and the fact that no central difference scheme of order-of-accuracy greater than two is time-stable for this system with strong BCs served as a motivation for the development of SAT (weak) BC approach in Carpenter *et al.* [11]. Here we evaluate the numerical stability and accuracy of various schemes with strong BC implementation.

The hyperbolic system, on domain  $0 \leq x \leq 1$  and  $t \geq 0$ , is given by

$$\frac{\partial U}{\partial t} + \frac{\partial U}{\partial x} = 0, \quad (55)$$

$$\frac{\partial V}{\partial t} - \frac{\partial V}{\partial x} = 0. \quad (56)$$

$$\text{Initial conditions :} \quad U(x, 0) = \sin 2\pi x, \quad V(x, 0) = -\sin 2\pi x. \quad (57)$$

$$\text{Boundary conditions :} \quad U(0, t) = V(0, t), \quad V(1, t) = U(1, t). \quad (58)$$

This system provides a strict test of numerical stability because it is neutrally stable, *i.e.*, the energy,  $\int_0^1 [U(x, t)^2 + V(x, t)^2] dx$ , remains constant with time.

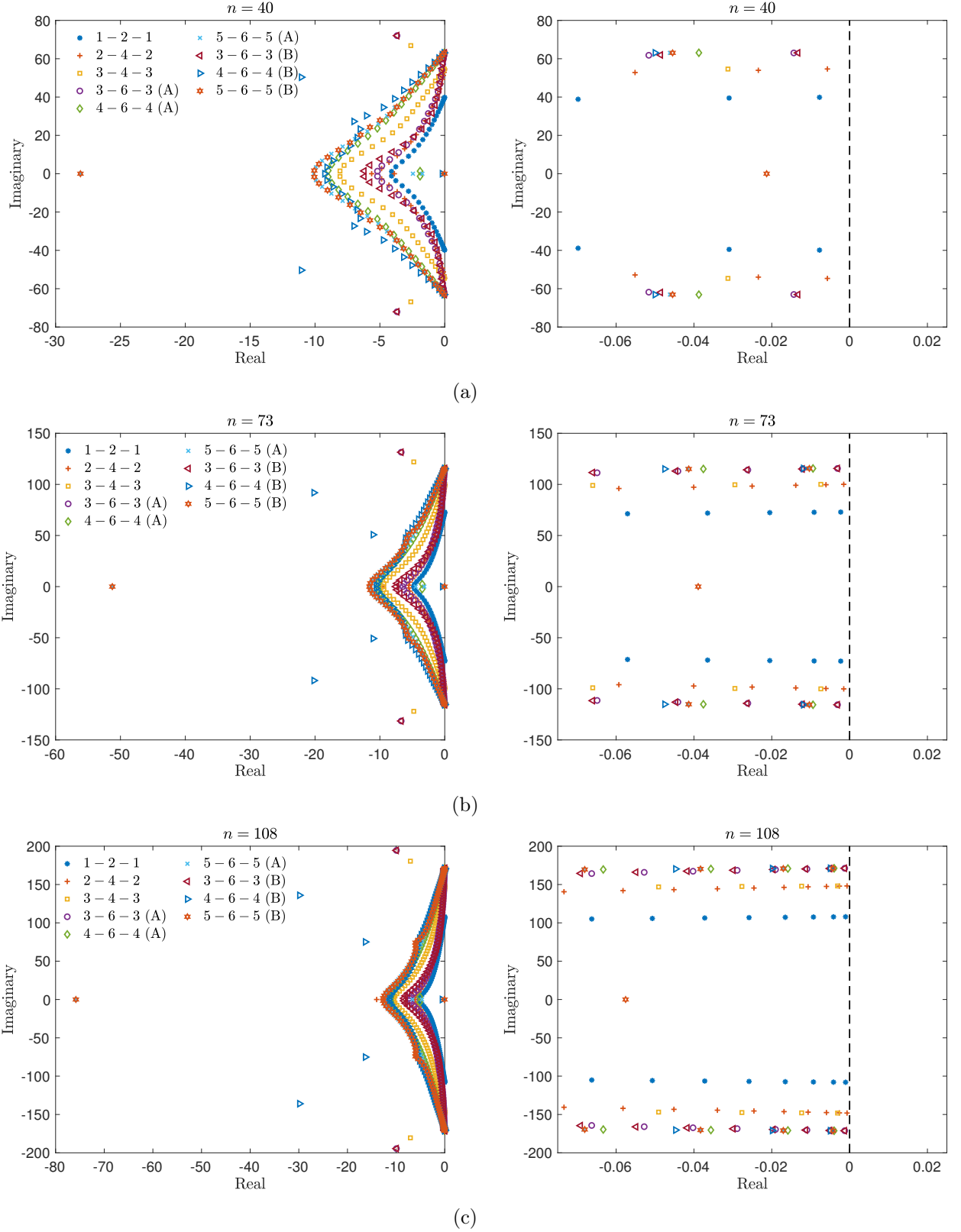


Figure 1: Eigenvalue spectrum of the system matrix to solve (1) with initial and boundary condition given by (53) using various schemes. The figures in the left column show all eigenvalues, whereas figures on the right column show a magnified view near the imaginary axis. Number of grid points: (a)  $n = 40$ , (b)  $n = 73$ , and (c)  $n = 108$ . Legend is the same for all plots.

$n$	1 – 2 – 1				2 – 4 – 2				3 – 4 – 3			
	$\log_{10} \ \varepsilon\ _2$	Rate	$\log_{10} \ \varepsilon\ _\infty$	Rate	$\log_{10} \ \varepsilon\ _2$	Rate	$\log_{10} \ \varepsilon\ _\infty$	Rate	$\log_{10} \ \varepsilon\ _2$	Rate	$\log_{10} \ \varepsilon\ _\infty$	Rate
20	-1.442427		-1.234263		-1.828907		-1.541334		-1.946005		-1.801309	
40	-2.044080	1.999	-1.834978	1.996	-2.789357	3.215	-2.335029	2.637	-3.355294	4.682	-3.137755	4.440
80	-2.644558	1.995	-2.435158	1.994	-3.729319	3.298	-3.204515	2.888	-4.706377	4.488	-4.522492	4.599
160	-3.245543	1.996	-3.039630	2.008	-4.653197	3.110	-4.099137	2.972	-5.978925	4.227	-5.810145	4.277
320	-3.846993	1.998	-3.646874	2.017	-5.567189	3.046	-5.000487	2.994	-7.208962	4.086	-7.047904	4.112
640	-4.448730	1.999	-4.250385	2.005	-6.475805	3.027	-5.903084	2.998	-8.418204	4.017	-8.233410	3.938
$n$	3 – 6 – 3 (A)				4 – 6 – 4 (A)				5 – 6 – 5 (A)			
	$\log_{10} \ \varepsilon\ _2$	Rate	$\log_{10} \ \varepsilon\ _\infty$	Rate	$\log_{10} \ \varepsilon\ _2$	Rate	$\log_{10} \ \varepsilon\ _\infty$	Rate	$\log_{10} \ \varepsilon\ _2$	Rate	$\log_{10} \ \varepsilon\ _\infty$	Rate
20	-1.898413		-1.583802		-1.664885		-1.450932		-2.262936		-1.675242	
40	-2.966704	3.549	-2.681008	3.645	-2.900505	4.105	-2.436262	3.273	-3.973581	5.683	-3.342266	5.538
80	-4.111979	3.805	-3.833491	3.828	-4.074842	3.901	-3.605665	3.885	-5.478018	4.998	-4.704660	4.526
160	-5.297396	3.938	-5.021512	3.947	-5.386930	4.359	-5.059455	4.829	-6.972898	4.966	-6.009887	4.336
320	-6.496099	3.982	-6.221023	3.985	-6.786594	4.650	-6.113276	3.501	-8.809748	6.102	-7.811266	5.984
640	-7.698613	3.995	-7.423758	3.995	-8.260190	4.895	-7.537892	4.732	-10.842165	6.752	-9.770531	6.509
$n$	3 – 6 – 3 (B)				4 – 6 – 4 (B)				5 – 6 – 5 (B)			
	$\log_{10} \ \varepsilon\ _2$	Rate	$\log_{10} \ \varepsilon\ _\infty$	Rate	$\log_{10} \ \varepsilon\ _2$	Rate	$\log_{10} \ \varepsilon\ _\infty$	Rate	$\log_{10} \ \varepsilon\ _2$	Rate	$\log_{10} \ \varepsilon\ _\infty$	Rate
20	-1.681300		-1.160180		-1.626908		-1.408395		-2.673249		-2.454826	
40	-3.107325	4.737	-2.484588	4.399	-2.918772	4.291	-2.686067	4.244	-4.446491	5.891	-4.243627	5.942
80	-4.493823	4.606	-3.853948	4.549	-4.164175	4.137	-3.966911	4.255	-6.382406	6.431	-6.169934	6.399
160	-5.775224	4.257	-5.200389	4.473	-5.384862	4.055	-5.232136	4.203	-8.272050	6.277	-8.123161	6.488
320	-7.002522	4.077	-6.504670	4.333	-6.613555	4.082	-6.421984	3.953	-10.126948	6.162	-9.976467	6.157
640	-8.213472	4.023	-7.770852	4.206	-7.878845	4.203	-7.665794	4.132				

Table 1:  $L_2$ – and  $L_\infty$ –norm of the solution error and convergence rates from solving (1) using various schemes. Error calculations performed at  $t = 1.0$ .



Let  $\mathbf{u}(t) = [u_0(t) \ \cdots \ \cdots \ u_n(t)]^T$  and  $\mathbf{v}(t) = [v_0(t) \ \cdots \ \cdots \ v_n(t)]^T$  denote the grid function, assuming a spatial discretization of the above system with  $n + 1$  grid points. A semi-discretization of (55)-(58) using strong boundary conditions is given by

$$\frac{d\mathbf{w}}{dt} = -\mathcal{D}\mathbf{w}, \quad (59)$$

where  $\mathbf{w}(t) = \begin{bmatrix} \tilde{\mathbf{u}}(t) & \tilde{\mathbf{v}}(t) \end{bmatrix}^T$  with  $\tilde{\mathbf{u}}(t) = [u_1(t) \ \cdots \ \cdots \ u_n(t)]^T$  and  $\tilde{\mathbf{v}}(t) = [v_0(t) \ \cdots \ \cdots \ v_{n-1}(t)]^T$ . The derivative operator,  $\mathcal{D}$ , is given by

$$\mathcal{D} = \begin{bmatrix} H & 0 \\ 0 & H^\# \end{bmatrix}^{-1} \begin{bmatrix} \tilde{Q} & Q_0 \\ -Q_0^\# & -\tilde{Q}^\# \end{bmatrix} = \mathcal{H}^{-1} \mathcal{Q},$$

where  $\tilde{Q}$  and  $Q_0$  are as described in (10) and (30), respectively, and the superscript  $\#$  denotes the matrix transformation (32). The off-diagonal entries of  $\mathcal{Q}$ , involving  $Q_0$ , apply the boundary conditions (58) strongly.

As mentioned earlier, existing high-order central difference schemes fail to be stable for this problem when solved with strong BCs. Figure 2(a) shows the eigenvalue spectrum of the system matrix, given by  $-\mathcal{D}$  in (59), for various high-order schemes from literature. All schemes exhibit eigenvalues with positive real part, therefore, the numerical solution grows non-physically in a long-time simulation, as shown by the solution error ( $\varepsilon$ ) plotted in Figure 2(b).

Figure 3 shows the the eigenvalue spectrum of the system matrix for various number of grid points using the EBC schemes that are time-stable for this problem, *i.e.*, where the eigenvalues lie in strict left half of the complex plane. The 1 – 2 – 1, 2 – 4 – 2, 3 – 4 – 3, 3 – 6 – 3 (B), 4 – 6 – 4 (B) and 5 – 6 – 5 (B) schemes are time-stable. The (A) schemes, as discussed in Sections 3.4, 3.5, and 3.6, and whose eigenvalue spectra are shown in Figure 4, exhibit eigenvalues with positive real part and, hence, they are not time-stable for this problem.

Table 2 shows the  $L_2$ - and  $L_\infty$ -norm of the solution error, denoted by  $\varepsilon$ , and the respective convergence rates from the time-stable schemes for this problem. All schemes converge with at least  $p_b + 1$  global order-of-accuracy, except the 4 – 6 – 4 scheme that shows an accuracy between 4 and 5. The  $n = 640$  values for the 5 – 6 – 5 (B) scheme are omitted on account of individual grid point errors approaching machine precision for such resolutions.

#### 4.3. Inviscid Burgers' equation

Consider the inviscid Burgers' equation with a source term,

$$\frac{\partial U}{\partial t} + \frac{\partial}{\partial x} \left( \frac{U^2}{2} \right) = f_U. \quad 0 \leq x \leq 1, \ t \geq 0, \quad (60)$$

The method of manufactured solutions [30] is employed to perform long-time simulations to assess the stability and accuracy of the derived schemes. The source term prevents solution discontinuities. The solution is assumed to be

$$U(x, t) = \sin 2\pi(x - t) + C, \quad (61)$$

where  $C = 1.0$  is a constant. (61) prescribes the initial and boundary data, and the source term is given by

$$f_U(x, t) = \pi \sin 4\pi(x - t). \quad (62)$$

The solution (61) is non-negative in the domain at all times, therefore, the boundary condition  $U(0, t) = \sin 2\pi(-t) + C$  makes the problem well-posed.

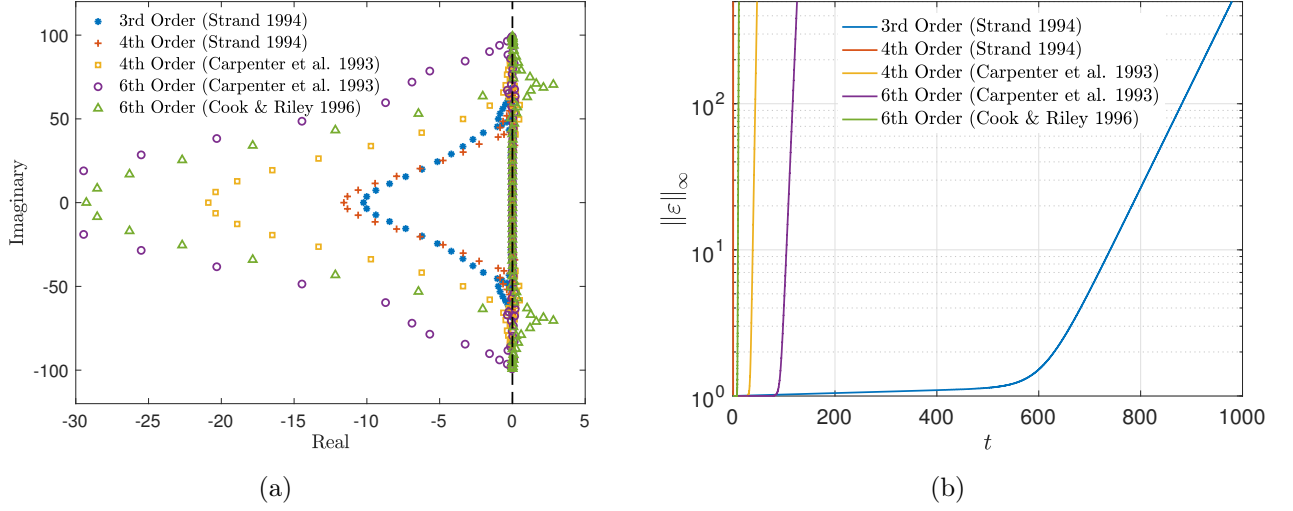


Figure 2: (a) Eigenvalue spectrum of the system matrix near imaginary axis and (b)  $L_\infty$ -error from solving the coupled hyperbolic system (55)-(58) using various spatial schemes from literature with strong boundary conditions. Classical RK4 is used for time integration with a CFL of 0.25 and 50 grid points in the domain. 3rd Order (Strand 1994) denotes the diagonal-norm stencil in [16, Appendix A] that is second-order accurate at the boundary; 4th Order (Strand 1994) denotes the minimum-bandwidth full-norm stencil in [16, Appendix B] that is third-order accurate at the boundary; 4th Order (Carpenter et al. 1993) and 6th Order (Carpenter et al. 1993) denote the  $4^3 - 4 - 4^3$  and  $5^2, 5^2 - 6 - 5^2, 5^2$  stencil of [28], respectively; 6th Order (Cook & Riley 1996) denotes the sixth-order compact scheme of [29, Section 7.3].

$n$	1 - 2 - 1				2 - 4 - 2				3 - 4 - 3			
	$\log_{10} \ \varepsilon\ _2$	Rate	$\log_{10} \ \varepsilon\ _\infty$	Rate	$\log_{10} \ \varepsilon\ _2$	Rate	$\log_{10} \ \varepsilon\ _\infty$	Rate	$\log_{10} \ \varepsilon\ _2$	Rate	$\log_{10} \ \varepsilon\ _\infty$	Rate
20	-1.217223		-1.225890		-1.676188		-1.508359		-1.771245		-1.777406	
40	-1.803716	1.948	-1.770808	1.810	-2.643277	3.215	-2.351858	2.802	-3.162562	4.622	-3.117156	4.451
80	-2.398761	1.977	-2.353810	1.937	-3.582599	3.120	-3.206750	2.840	-4.494335	4.424	-4.487070	4.551
160	-2.997715	1.990	-2.955241	1.998	-4.505004	3.064	-4.099017	2.964	-5.760716	4.207	-5.754529	4.210
320	-3.598344	1.995	-3.555882	1.995	-5.417936	3.035	-5.000116	2.993	-6.983890	4.063	-6.979341	4.069
640	-4.199721	1.998	-4.157098	1.997	-6.325949	3.016	-5.902821	2.999	-8.083748	3.654	-8.059036	3.587
$n$	3 - 6 - 3 (B)				4 - 6 - 4 (B)				5 - 6 - 5 (B)			
	$\log_{10} \ \varepsilon\ _2$	Rate	$\log_{10} \ \varepsilon\ _\infty$	Rate	$\log_{10} \ \varepsilon\ _2$	Rate	$\log_{10} \ \varepsilon\ _\infty$	Rate	$\log_{10} \ \varepsilon\ _2$	Rate	$\log_{10} \ \varepsilon\ _\infty$	Rate
20	-1.992622		-1.811695		-1.475772		-1.408130		-2.504425		-2.452328	
40	-3.419956	4.742	-3.201140	4.616	-2.768026	4.293	-2.685970	4.245	-4.298931	5.961	-4.287300	6.096
80	-4.765353	4.469	-4.638031	4.773	-4.013613	4.138	-3.966871	4.255	-6.229548	6.413	-6.201685	6.359
160	-6.020126	4.168	-5.970614	4.427	-5.234341	4.055	-5.232135	4.203	-8.116139	6.267	-8.115883	6.359
320	-7.237780	4.045	-7.187086	4.041	-6.463043	4.082	-6.421990	3.953	-9.969169	6.156	-9.967690	6.152
640	-8.445220	4.011	-8.394934	4.012	-7.728336	4.203	-7.665802	4.132				

Table 2:  $L_2$ - and  $L_\infty$ -norm of the solution error and convergence rates from solving (55)-(58) using various schemes. Error calculations performed at  $t = 1.0$ .

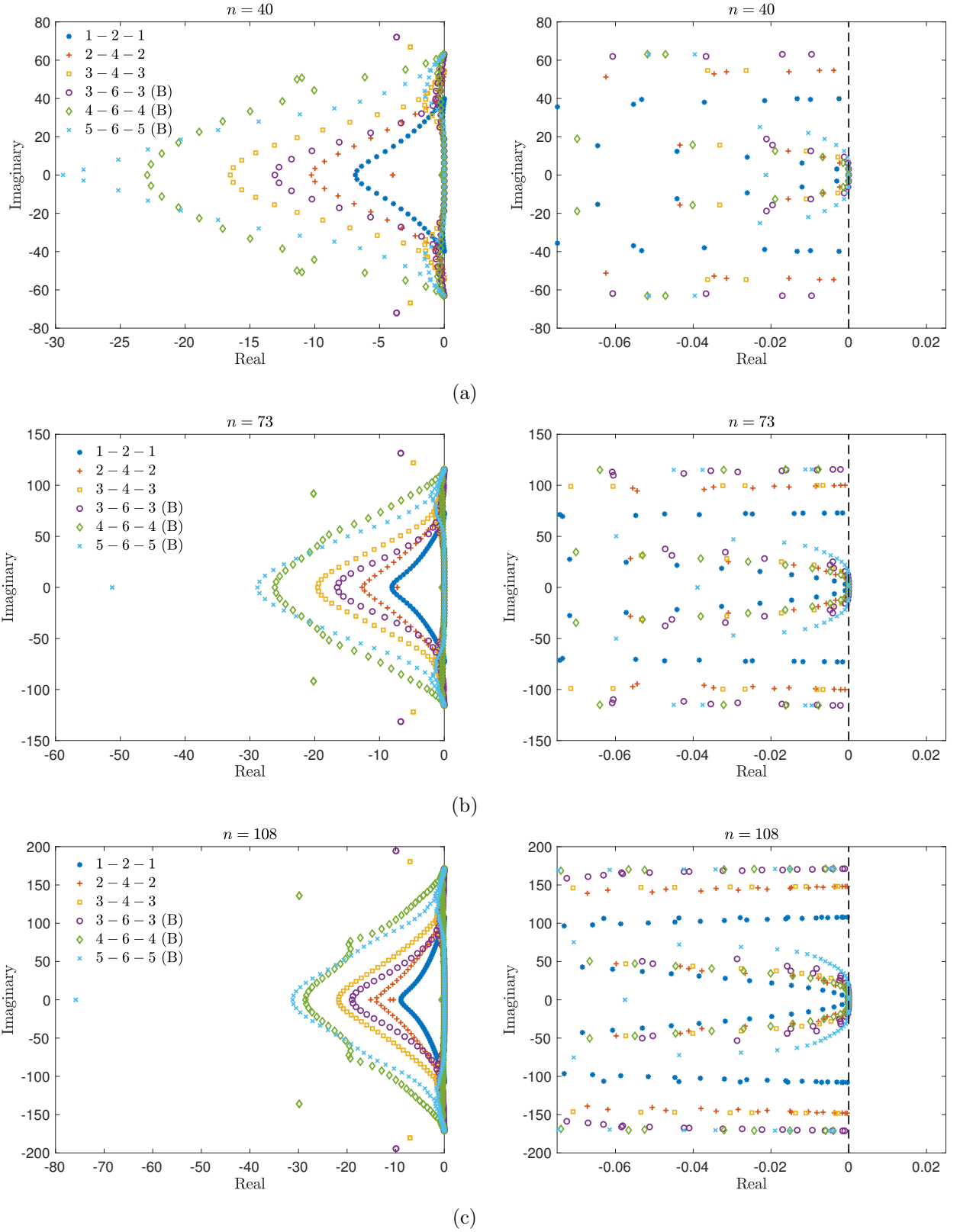


Figure 3: Eigenvalue spectrum of the system matrix to solve (55)-(58) using various schemes. The figures in the left column show all eigenvalues, whereas figures on the right column show a magnified view near the imaginary axis. Number of grid points: (a)  $n = 40$ , (b)  $n = 73$ , and (c)  $n = 108$ . Legend is the same for all plots..

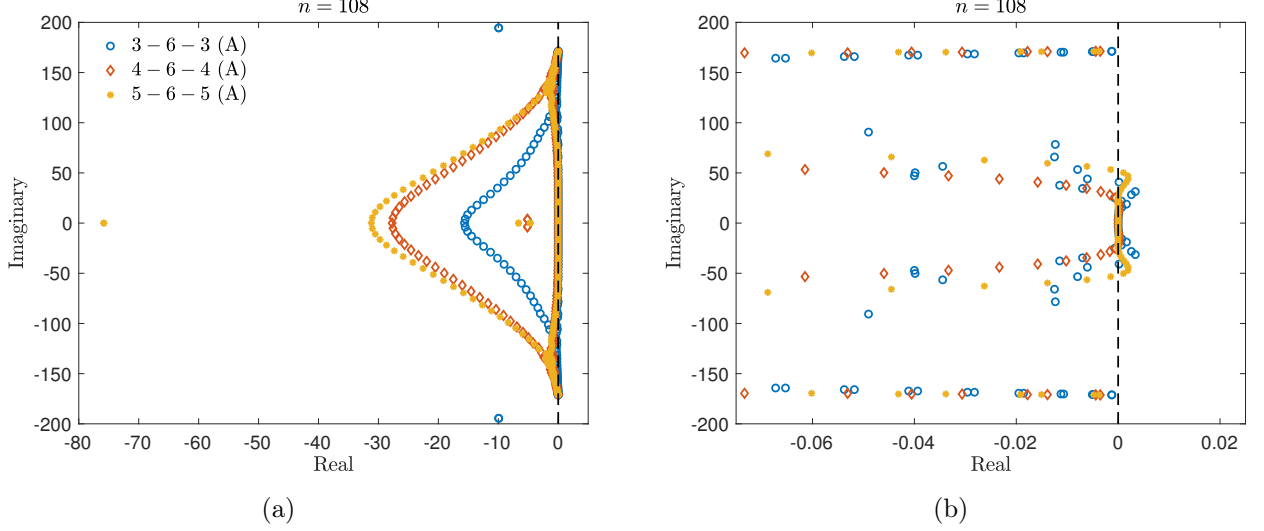


Figure 4: Eigenvalue spectrum of the system matrix to solve (55)-(58) using (A) schemes of Appendix B and  $n = 108$ . (a) All eigenvalues, (b) Magnified view near the imaginary axis. Legend is the same for both plots.

Figure 5 shows the  $L_\infty$ -errors with time in long-time simulations using various schemes with various number of grid points. A constant error profile indicates time-stable behavior. Figures 5(a)-(c) show errors from the EBC schemes that are time-stable for this problem. All schemes, except the 4-6-4 (A) and 5-6-5 (A) schemes, show time-stability. For comparison, Figure 5(d) shows the errors from the schemes (from literature) used in Figure 2 with  $n = 40$ . Results for higher  $n$  were similar with regards to time-stability. While all the schemes were unstable with strong BC implementation for the coupled system of Section 4.2, the diagonal-norm 3rd-order scheme of [16] and the 4th-order compact scheme of [28] show time-stability for this problem. The other schemes diverge early in time.

Table 3 shows the  $L_2$ - and  $L_\infty$ -norm of the solution error and the respective convergence rates from the time-stable EBC schemes for this problem. All schemes show at least  $p_b + 1$  global order-of-accuracy, except the 4-6-4 scheme that, like in the previous sections, exhibits an accuracy between 4 and 5.

#### 4.4. 2-D variable-coefficient advection equation

Consider the scalar problem

$$\begin{aligned} \frac{\partial \phi}{\partial t} + u \frac{\partial \phi}{\partial x} + v \frac{\partial \phi}{\partial y} &= 0, \quad 0 \leq x, y \leq L \quad t \geq 0, \\ u(x, y) &= \frac{\partial r}{\partial x}, \quad v(x, y) = \frac{\partial r}{\partial y}, \\ r(x, y) &= \sqrt{(x - x_0)^2 + (y - y_0)^2}, \end{aligned} \tag{63}$$

where  $L = \sqrt{2}$ ,  $x_0 = -0.25$  and  $y_0 = -0.25$ . The initial and boundary conditions are given by

$$\phi(x, y, 0) = \sin 2\pi r, \tag{64}$$

and

$$\phi(0, y, t) = \sin 2\pi (r(0, y) - t), \quad \phi(x, 0, t) = \sin 2\pi (r(x, 0) - t), \tag{65}$$

respectively. The exact solution to the problem is  $\phi(x, y, t) = \sin 2\pi (r - t)$ .

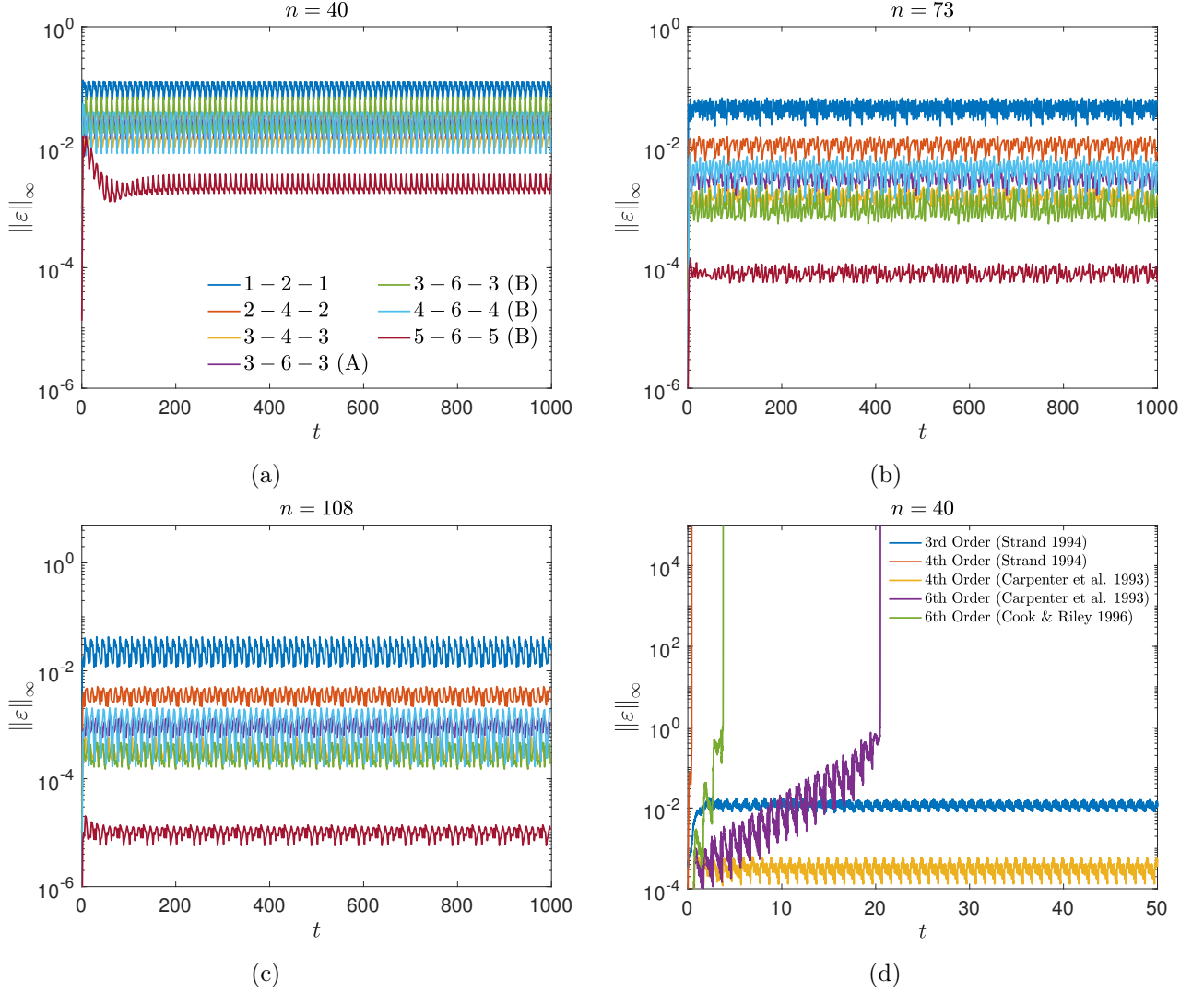


Figure 5:  $L_\infty$ -error from long-time simulations of (60) using various schemes with (a)  $n = 40$ , (b)  $n = 73$ , and (c)  $n = 108$ . Subfigure (d) shows errors from simulations using the schemes (from literature) referenced in Figure 2 and  $n = 40$ . Legend is the same in subfigures (a), (b) and (c). Note the difference in axis scales between subfigure (d) and other subfigures.

$n$	1 – 2 – 1				2 – 4 – 2				3 – 4 – 3			
	$\log_{10} \ \varepsilon\ _2$	Rate	$\log_{10} \ \varepsilon\ _\infty$	Rate	$\log_{10} \ \varepsilon\ _2$	Rate	$\log_{10} \ \varepsilon\ _\infty$	Rate	$\log_{10} \ \varepsilon\ _2$	Rate	$\log_{10} \ \varepsilon\ _\infty$	Rate
20	-1.176427		-0.738973		-1.987098		-1.528051		-2.222065		-1.804324	
40	-1.781249	2.009	-1.280048	1.797	-2.833219	2.811	-2.230067	2.332	-3.540079	4.378	-2.998817	3.968
80	-2.414563	2.104	-1.740013	1.528	-3.677578	2.805	-3.068572	2.785	-4.765848	4.072	-4.154203	3.838
160	-3.042268	2.085	-2.244332	1.675	-4.547528	2.890	-3.765753	2.316	-6.170204	4.665	-5.414077	4.185
320	-3.658045	2.046	-2.793888	1.826	-5.397666	2.824	-4.496024	2.426	-7.502206	4.425	-6.640841	4.075
640	-4.268635	2.028	-3.375075	1.931	-6.297327	2.989	-5.369695	2.902	-8.748263	4.139	-7.871633	4.089
$n$	3 – 6 – 3 (A)				3 – 6 – 3 (B)				4 – 6 – 4 (B)			
	$\log_{10} \ \varepsilon\ _2$	Rate	$\log_{10} \ \varepsilon\ _\infty$	Rate	$\log_{10} \ \varepsilon\ _2$	Rate	$\log_{10} \ \varepsilon\ _\infty$	Rate	$\log_{10} \ \varepsilon\ _2$	Rate	$\log_{10} \ \varepsilon\ _\infty$	Rate
20	-2.480441		-2.206364		-2.437228		-2.136384		-2.375836		-1.988546	
40	-3.395410	3.039	-2.829500	2.070	-3.463385	3.409	-2.876606	2.459	-3.595080	4.050	-3.003636	3.372
80	-4.508041	3.696	-3.930992	3.659	-4.686090	4.062	-4.306489	4.750	-4.780893	3.939	-4.147072	3.798
160	-5.703416	3.971	-5.085232	3.834	-5.876633	3.955	-5.540050	4.098	-6.092379	4.357	-5.414182	4.209
320	-6.898507	3.970	-6.199627	3.702	-7.068063	3.958	-6.705179	3.870	-7.381408	4.282	-6.640851	4.075
640	-8.101203	3.995	-7.347446	3.813	-8.264577	3.975	-7.884398	3.917	-8.655121	4.231	-7.876042	4.103
$n$	5 – 6 – 5 (B)											
	$\log_{10} \ \varepsilon\ _2$	Rate	$\log_{10} \ \varepsilon\ _\infty$	Rate								
20	-3.153152		-2.596112									
40	-5.262497	7.007	-4.606102	6.677								
80	-6.471753	4.017	-5.738427	3.762								
160	-8.386054	6.359	-7.574293	6.099								
320	-10.426924	6.780	-9.477772	6.323								

Table 3:  $L_2$ - and  $L_\infty$ -norm of the solution error and convergence rates from solving (60) using various schemes. Error calculations performed at  $t = 1.0$ .

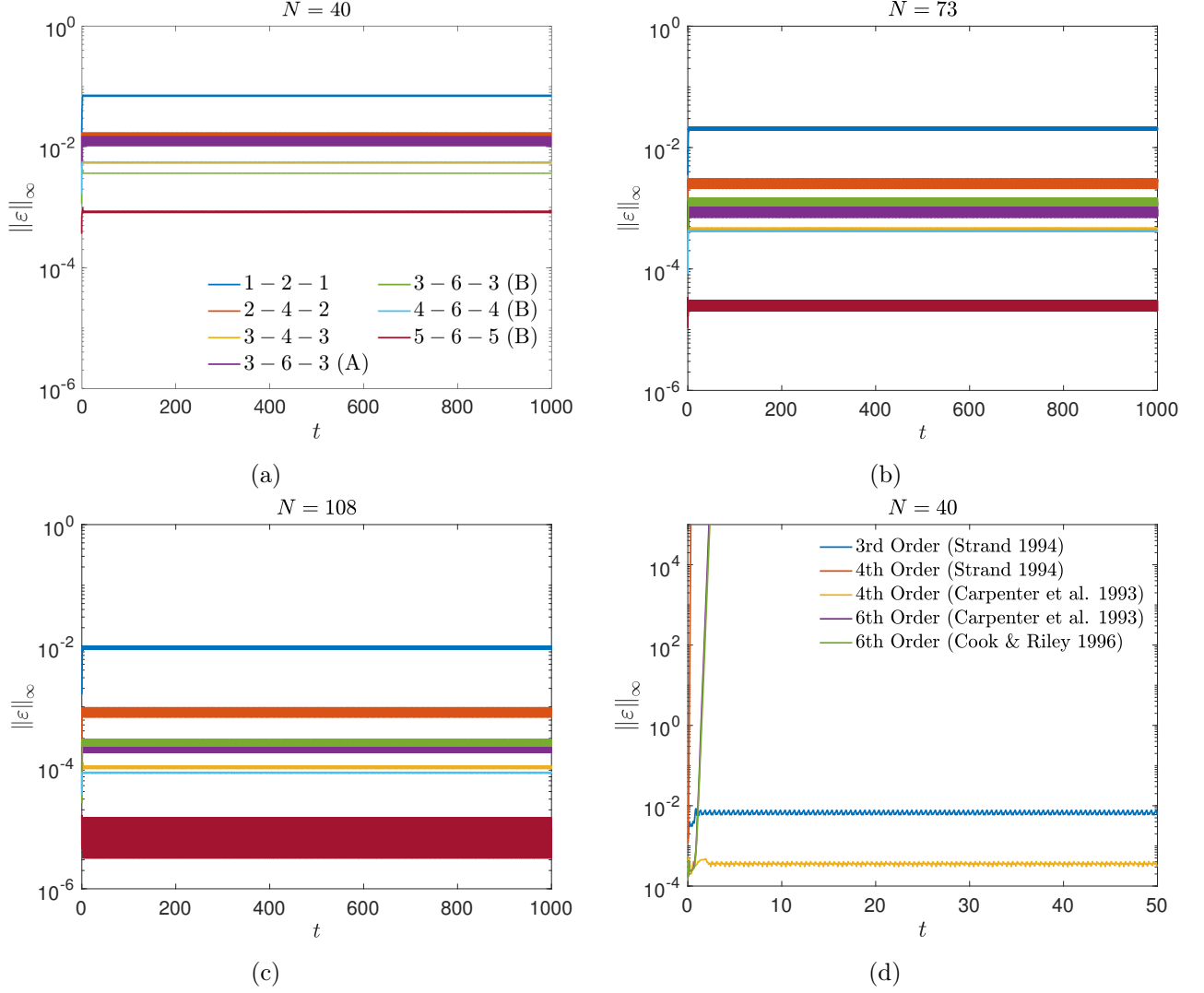


Figure 6:  $L_\infty$ -error from long-time simulations of (63)-(65) using various schemes with (a)  $N = 40$ , (b)  $N = 73$ , and (c)  $N = 108$ . Subfigure (d) shows errors from simulations using the schemes (from literature) referenced in Figure 2 and  $N = 40$ . Legend is the same in subfigures (a), (b) and (c). Note the difference in axis scales between subfigure (d) and other subfigures.

Figure 6 shows the  $L_\infty$ -errors from long-time simulations of (63)-(65) using various schemes with  $N \times N$  grid points. To highlight the efficacy of the derived schemes, a CFL of 1.5, calculated from

$$\text{CFL} = \Delta t \left( \frac{|u|}{\Delta x} + \frac{|v|}{\Delta y} \right),$$

is used for the results of this figure. Figures 6(a)-(c) show errors from the EBC schemes that are time-stable for this problem. All schemes, except the  $4 - 6 - 4$  (A) and  $5 - 6 - 5$  (A) schemes, show time-stability, as was the case in the previous section. For comparison, Figure 6(d) shows errors from the schemes used in Figure 2 for  $N = 40$ . As in the case of inviscid Burgers' equation in previous section, the diagonal-norm 3rd-order scheme of [16] and the 4th-order compact scheme of [28] show time-stability. The other schemes tend to diverge very early in time.

Table 4 shows the  $L_2$ - and  $L_\infty$ -norm of the solution error and the respective convergence rates from the time-stable EBC schemes for this problem. All schemes show at least  $p_b + 1$  global order-of-accuracy, except the  $4 - 6 - 4$  scheme that exhibits an accuracy between 4 and 5.

$N$	1 – 2 – 1				2 – 4 – 2				3 – 4 – 3			
	$\log_{10} \ \varepsilon\ _2$	Rate	$\log_{10} \ \varepsilon\ _\infty$	Rate	$\log_{10} \ \varepsilon\ _2$	Rate	$\log_{10} \ \varepsilon\ _\infty$	Rate	$\log_{10} \ \varepsilon\ _2$	Rate	$\log_{10} \ \varepsilon\ _\infty$	Rate
30	-1.404196		-1.037912		-2.118175		-1.439252		-2.337262		-1.760082	
60	-2.018962	1.993	-1.615432	1.872	-3.092760	3.160	-2.445756	3.263	-3.646564	4.245	-2.929111	3.790
120	-2.626948	1.995	-2.207732	1.944	-4.035679	3.095	-3.435688	3.249	-4.956536	4.299	-4.123419	3.920
240	-3.232256	1.999	-2.801850	1.962	-4.954626	3.034	-4.343758	2.998	-6.268282	4.331	-5.324285	3.965
$N$	3 – 6 – 3 (A)				3 – 6 – 3 (B)				4 – 6 – 4 (B)			
	$\log_{10} \ \varepsilon\ _2$	Rate	$\log_{10} \ \varepsilon\ _\infty$	Rate	$\log_{10} \ \varepsilon\ _2$	Rate	$\log_{10} \ \varepsilon\ _\infty$	Rate	$\log_{10} \ \varepsilon\ _2$	Rate	$\log_{10} \ \varepsilon\ _\infty$	Rate
30	-2.226785		-1.703267		-2.513605		-1.942708		-2.168196		-1.669679	
60	-3.432703	3.910	-2.746027	3.381	-3.838707	4.296	-3.070683	3.657	-3.497300	4.309	-3.017642	4.370
120	-4.624781	3.912	-3.806925	3.482	-5.147756	4.296	-4.249164	3.868	-4.736518	4.067	-4.278298	4.137
240	-5.826513	3.968	-4.994472	3.921	-6.456819	4.322	-5.447414	3.957	-5.965303	4.057	-5.521588	4.105

$N$	5 – 6 – 5 (B)			
	$\log_{10} \ \varepsilon\ _2$	Rate	$\log_{10} \ \varepsilon\ _\infty$	Rate
30	-3.075453		-2.591346	
60	-4.829965	5.688	-4.251557	5.382
120	-6.638466	5.935	-5.944372	5.556
240	-8.482509	6.089	-7.679641	5.730

Table 4:  $L_2$ – and  $L_\infty$ –norm of the solution error and convergence rates from solving (63)-(65) on a  $N \times N$  grid using various schemes. Error calculations performed at  $t = 1.0$ .

## 5. Application to the Euler equations using characteristic boundary conditions

This section discusses the application of the schemes derived in Section (3) to solve the two-dimensional Euler equations. The extension to three-dimensions follows a similar approach. The two-dimensional Euler equations, assuming a calorically perfect gas, in generalized coordinates are given by

$$\frac{\partial \mathbf{Q}}{\partial \tau} + \frac{\partial \mathbf{F}}{\partial \xi} + \frac{\partial \mathbf{G}}{\partial \eta} = 0, \quad (66)$$

$$\mathbf{Q} = \frac{1}{J} \begin{bmatrix} \rho \\ \rho u \\ \rho v \\ \rho E \end{bmatrix}, \quad \mathbf{F} = \frac{1}{J} \begin{bmatrix} \rho U \\ \rho u U + \xi_x p \\ \rho v U + \xi_y p \\ \rho E U + \xi_{x_i} u_i p \end{bmatrix}, \quad \mathbf{G} = \frac{1}{J} \begin{bmatrix} \rho V \\ \rho u V + \eta_x p \\ \rho v V + \eta_y p \\ \rho E V + \eta_{x_i} u_i p \end{bmatrix}, \quad (67)$$

$$U = \xi_t + \xi_x u + \xi_y v, \quad V = \eta_t + \eta_x u + \eta_y v,$$

$$\rho E = \frac{p}{\gamma - 1} + \rho \left( \frac{u^2 + v^2}{2} \right).$$

The coordinate transformation between the physical domain  $\mathbf{x} = (x, y)$  and the computational domain  $\boldsymbol{\xi} = (\xi, \eta)$  is  $\boldsymbol{\xi} = \boldsymbol{\Xi}(\mathbf{x}, t)$  with the inverse transformation  $\mathbf{x} = \mathbf{X}(\boldsymbol{\xi}, \tau)$  and the metric Jacobian  $J = \det(\partial \boldsymbol{\xi} / \partial \mathbf{x}) = (x_\xi y_\eta - x_\eta y_\xi)^{-1}$ . We assume the time to be invariant, therefore,  $\tau = t$ .  $u, v$  are the Cartesian velocity components,  $\rho$  denotes the density,  $p$  the pressure, and  $E$  is the total energy per unit mass.

Let  $i$  and  $j$  denote the grid indices in  $\xi$  and  $\eta$  direction, respectively, where  $0 \leq i \leq N_\xi$  and  $0 \leq j \leq N_\eta$  for a  $(N_\xi + 1) \times (N_\eta + 1)$  computational grid. To simplify the discussion, let us consider the boundary located at  $i = 0$ , which has a constant  $\xi$  value. The flux-derivative in the  $\xi$ -direction in (66), then, has to be modified to account for the physical boundary condition. (66) can be transformed to a characteristic form in the direction normal to the  $i = 0$  boundary by using a similarity transformation  $A = \partial \mathbf{F} / \partial \mathbf{Q} = T_\xi \Lambda_\xi T_\xi^{-1}$ , where the columns of  $T_\xi$  contain the right eigenvectors of  $A$  and  $\Lambda_\xi$  is a diagonal matrix containing the



eigenvalues of  $A$ . The expressions for  $\Lambda_\xi$  and  $T_\xi$  can be found in [31]. The resulting characteristic equations are given by (e.g. [32])

$$\frac{\partial \mathbf{R}}{\partial t} + \mathbf{L} = \mathbf{S}_C, \quad (68)$$

where  $\mathbf{R}$  is the vector of characteristic variables,

$$\mathbf{L} = JT_\xi^{-1} \left\{ \frac{\partial \mathbf{F}}{\partial \xi} - \left[ \mathbf{F} \frac{\partial}{\partial \xi} \left( \frac{\xi_x}{J} \right) + \mathbf{G} \frac{\partial}{\partial \xi} \left( \frac{\xi_y}{J} \right) \right] \right\} \quad \text{and} \quad \mathbf{S}_C = -JT_\xi^{-1} \left\{ \frac{\partial \mathbf{G}}{\partial \eta} + \left[ \mathbf{F} \frac{\partial}{\partial \xi} \left( \frac{\xi_x}{J} \right) + \mathbf{G} \frac{\partial}{\partial \xi} \left( \frac{\xi_y}{J} \right) \right] \right\}. \quad (69)$$

The square brackets in (69) preserve the conservative form of the equation [32].

Following the one-dimensional discretization described in Section 2, a semi-discretization of (66) at grid points within the boundary-stencil depth from the  $i = 0$  boundary, i.e.,  $0 \leq i \leq \kappa$ , can be written as

$$\frac{dq_{ij}}{dt} = - \left( \frac{1}{J} S_\xi \mathbf{L}^* + \left[ \mathbf{F} \frac{\partial}{\partial \xi} \left( \frac{\xi_x}{J} \right) + \mathbf{G} \frac{\partial}{\partial \xi} \left( \frac{\xi_y}{J} \right) \right]_{ij} \right) - (D_\eta \mathbf{g})_{ij}, \quad (70)$$

where  $q_{ij}$  and  $(D_\eta \mathbf{g})_{ij}$  are the discrete approximations of  $\mathbf{Q}$  and  $\partial \mathbf{G} / \partial \eta$  at  $i, j$  grid point and  $\mathbf{L}^*$  denotes the modified characteristic convection term in  $\xi$ -direction given by

$$\mathbf{L}^* = \mathbf{L}_{\text{SBP}}^* + \mathbf{L}_{\text{EBC}}^*. \quad (71)$$

The derivative operators derived in Section 3 to satisfy the stability and conservation constraints of Section 2 are non-square and use different stencils at inflow (where physical boundary condition is applied) and outflow boundaries. The outflow boundary uses an SBP stencil, whereas stencils for the inflow boundary (that are different from SBP stencils) will be referred to as EBC stencils.  $\mathbf{L}_{\text{SBP}}^*$  denotes the convection terms for the outgoing waves calculated using the SBP stencil. The outgoing characteristics correspond to the negative entries of  $\Lambda_\xi$  at  $i = 0$  boundary, therefore, the elements of  $\mathbf{L}_{\text{SBP}}^*$  can be obtained from

$$(\mathbf{L}_{\text{SBP}}^*)_k = \frac{|\lambda_k| - \lambda_k}{2|\lambda_k|} (\mathbf{L}_{\text{SBP}})_k, \quad (72)$$

where  $(\bullet)_k$  denotes the  $k$ -th entry of the vector,  $\lambda_k$  is the  $k$ -th diagonal entry of  $\Lambda_\xi$  and  $\mathbf{L}_{\text{SBP}}$  is  $\mathbf{L}$  in (69) calculated using the SBP derivative approximation. The prefactor  $\frac{|\lambda_k| - \lambda_k}{2|\lambda_k|}$  ensures that the SBP stencil is applied only to the outgoing characteristic calculations.  $\mathbf{L}_{\text{EBC}}^*$  denotes the incoming characteristic convection terms that at  $i = 0$  are calculated using the physical boundary data and at  $0 < i \leq \kappa$  calculated using the EBC derivative stencils from

$$(\mathbf{L}_{\text{EBC}}^*)_k = \frac{|\lambda_k| + \lambda_k}{2|\lambda_k|} (\mathbf{L}_{\text{EBC}})_k, \quad (73)$$

where the expressions are as described for (72).

Next, we describe the application of the above discretization to solve problems where the exact or target boundary data for all conservative variables may or may not be known. The metric terms are calculated using the SBP derivative approximation and time integration is performed using the classical fourth-order Runge-Kutta (RK4) method with a CFL of 0.6 for all results discussed in the following sections. For convergence studies, the time step is taken small enough such that the temporal errors are insignificant compared to the spatial truncation errors.

### 5.1. Isentropic convecting vortex

The two-dimensional Euler equations are solved for a compressible isentropic vortex propagation. Initial and boundary conditions are applied using the exact solution given by

$$\begin{aligned} \rho &= \left( 1 - \frac{\varpi^2(\gamma - 1)}{8\pi^2 c_0^2} e^{1 - \varphi^2 r^2} \right)^{\frac{1}{\gamma - 1}}, & u &= u_0 - \frac{\varpi}{2\pi} \varphi (y - y_0 - v_0 t) e^{\frac{1 - \varphi^2 r^2}{2}}, \\ v &= v_0 + \frac{\varpi}{2\pi} \varphi (x - x_0 - u_0 t) e^{\frac{1 - \varphi^2 r^2}{2}}, & E &= \frac{p}{\gamma - 1} + \frac{1}{2} \rho (u^2 + v^2), \\ p &= \rho^\gamma, & r^2 &= (x - x_0 - u_0 t)^2 + (y - y_0 - v_0 t)^2, \end{aligned} \quad (74)$$

where  $(x_0, y_0)$  denotes the initial position of the vortex,  $(u_0, v_0)$  denotes the vortex convective velocity,  $\varphi$  is a scaling factor and  $\varpi$  denotes the non-dimensional circulation.  $\gamma = 1.4$ ,  $\varphi = 11$  and  $\varpi = 1$  is used for all simulations. All quantities in (74) are non-dimensional, obtained from the density scale  $= \rho_0^*$ , velocity scale  $u_0^* = \frac{c_0^*}{\sqrt{\gamma}}$ , unit length scale and pressure scale  $= \rho_0^* u_0^{*2}$ , where  $*$  denotes the dimensional quantities. The non-dimensional ambient speed of sound is  $c_0 = \sqrt{\gamma}$ .

Figure 8 shows the  $L_\infty$ -errors of velocity magnitude and density from simulations using  $(x_0, y_0) = (-1.5, 0)$  on the domain shown in Figure 7, *i.e.*, the vortex is initially located outside the computational domain. A subsonic ( $u_0 = 1.0, v_0 = 0$ ) and a supersonic ( $u_0 = 2.0, v_0 = 0$ ) convective velocity is used to examine the robustness of boundary implementation. In the subsonic case, the left/right boundary has three/one incoming and one/three outgoing characteristics. As per the characteristic eigenvalue/eigenvector matrices of [31], for the subsonic left boundary, the outgoing wave  $(\mathbf{L}^*)_4 = (\mathbf{L}_{\text{SBP}})_4$ , the incoming waves  $(\mathbf{L}^*)_{1,2,3}$  are calculated directly from the exact solution at  $i = 0$  and  $(\mathbf{L}^*)_{1,2,3} = (\mathbf{L}_{\text{EBC}})_{1,2,3}$  at  $0 < i \leq \kappa$ . For the subsonic right boundary, the outgoing waves  $(\mathbf{L}^*)_{1,2,3} = (\mathbf{L}_{\text{SBP}})_{1,2,3}$ , the incoming wave  $(\mathbf{L}^*)_4$  is calculated from the exact solution at  $i = N_x = N_\xi$  and  $(\mathbf{L}^*)_4 = (\mathbf{L}_{\text{EBC}})_4$  at  $N_\xi - \kappa \leq i < N_\xi$ . A similar characteristic treatment is used for the boundaries in the  $y$ -direction, where the incoming/outgoing waves at a boundary point are determined by the local entries of  $\Lambda_\eta$ , obtained from the similarity transformation  $B = \partial \mathbf{G} / \partial \mathbf{Q} = T_\eta \Lambda_\eta T_\eta^{-1}$  [31]. The supersonic case has characteristic velocities of the same sign at each  $x$ -boundary, therefore, theoretically, no similarity transformation is required to impose the boundary conditions. However, the code implementation performs a decomposition and assigns  $\mathbf{L}^* = \mathbf{L}_{\text{SBP}}$  at the right boundary and, at the left boundary,  $\mathbf{L}^*$  is calculated directly from the exact solution at  $i = 0$  and  $\mathbf{L}^* = \mathbf{L}_{\text{EBC}}$  at  $0 < i \leq \kappa$ .

In the simulation duration shown in Figure 8, the vortex enters and exits the domain through the left and the right boundary, respectively. The two spikes in the plots of Figure 8 mark the time of vortex entry and exit. The time interval between the entry and the exit is longer for the subsonic case, as expected. The vortex entry/exit triggers numerical reflections from the inflow/outflow boundary, which can be a source of instability and, therefore, the simulation is setup to examine if the errors grow with time. All schemes, except the 4 – 6 – 4(A) and 5 – 6 – 5(A) schemes, are stable for this problem. The error decay rate is higher in the supersonic cases, likely, because of the simpler boundary treatment where all characteristic eigenvalues have the same sign.

For comparison, density errors from the schemes taken from literature, referenced in Figure 2, are shown in Figure 9. Same flow parameters and characteristic boundary treatment that uses the exact solution as boundary condition as in Figure 8 is used for these runs. All schemes, except the diagonal-norm 3rd-order accurate scheme of [16], are unstable.

The extent/magnitude of numerical reflections at outflow boundary may depend on flow direction at the boundary [33]. To examine the robustness of the developed schemes, several numerical tests were performed with vortex traveling in a direction that is oblique to the boundary. Figure 10 shows the velocity magnitude and density errors with time for a subsonic vortex traveling through the top-right corner of computational domain. Initial vortex location  $(x_0, y_0) = (0, 0)$  with convective velocity  $(u_0 = 0.8, v_0 = 0.4)$  allow the vortex to exit the domain in  $t \lesssim 2$ , allowing an assessment of error growth with time. Figure 10 shows the results from EBC schemes that were stable for this problem. All schemes, except the 4 – 6 – 4(A) and 5 – 6 – 5(A) scheme, remain stable.

$L_2$ - and  $L_\infty$ -norm of the solution error and respective convergence rates from the stable schemes for this problem are given in Table 5. The errors are calculated at  $t = 1$  using  $(x_0, y_0) = (-0.5, 0)$  for the subsonic ( $u_0 = 1.0$ ) case. All schemes exhibit a global order-of-accuracy approaching  $p_b + 1$  or higher.

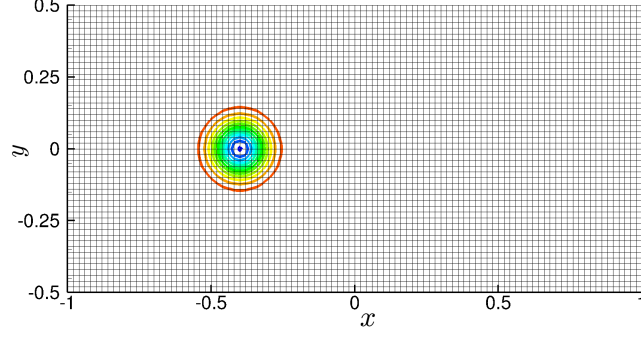


Figure 7: Computational domain for isentropic convective vortex simulations.

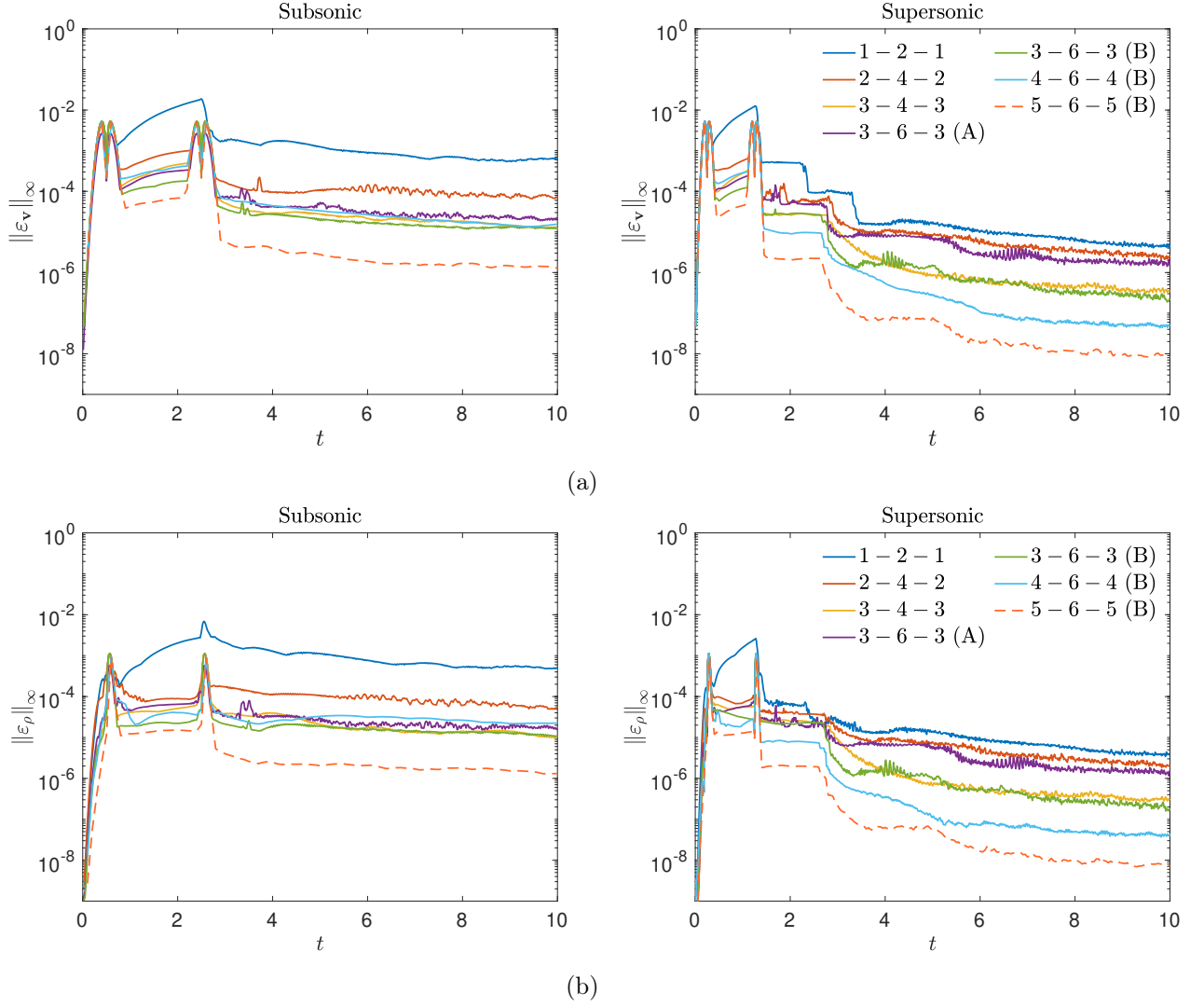


Figure 8:  $L_\infty$ -norm of (a) velocity magnitude error and (b) density error from solving the Euler equations for isentropic convecting vortex using various EBC schemes with  $201 \times 101$  grid points. Left and right columns show errors from a subsonic ( $u_0 = 1.0$ ,  $v_0 = 0$ ) and supersonic ( $u_0 = 2.0$ ,  $v_0 = 0$ ) convective velocity, respectively. Initial vortex location is  $(x_0, y_0) = (-1.5, 0)$  for all simulations. Legend is the same for all plots.

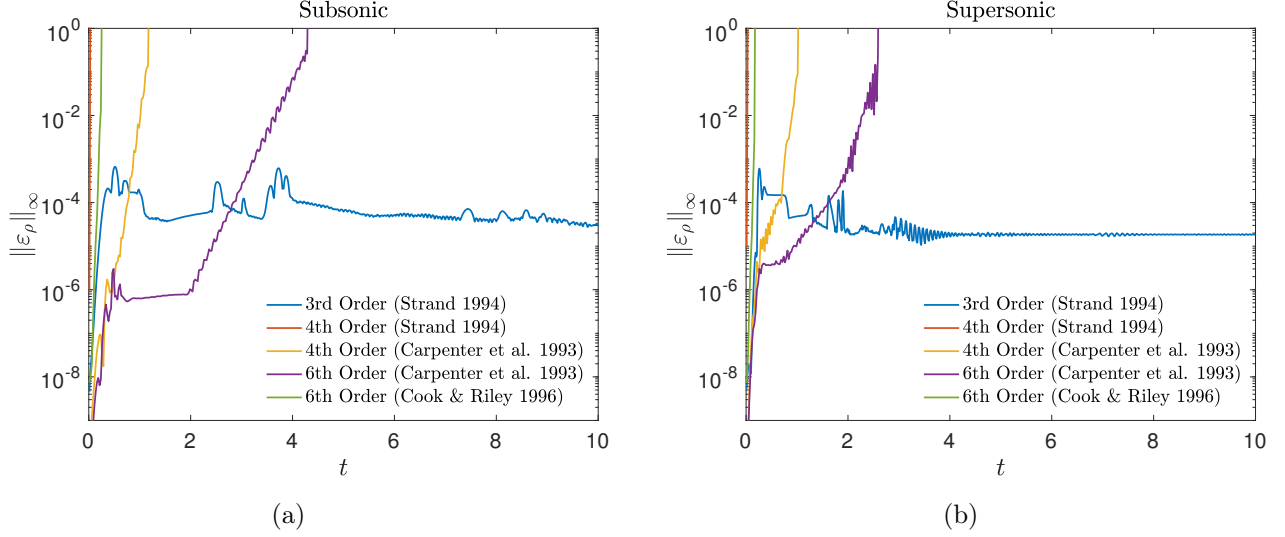


Figure 9:  $L_\infty$ -norm of density error from isentropic convecting vortex simulations using the schemes from literature with  $201 \times 101$  grid points and (a) subsonic ( $u_0 = 1.0, v_0 = 0$ ), (b) supersonic ( $u_0 = 1.0, v_0 = 0$ ) convective velocity. Initial vortex location is  $(x_0, y_0) = (-1.5, 0)$  for all simulations.

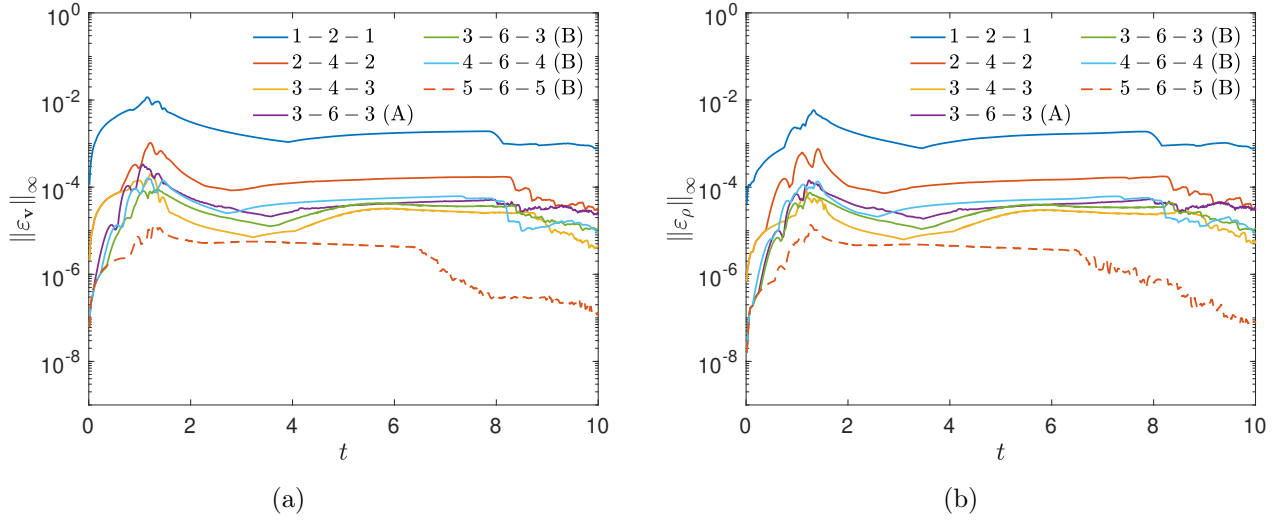


Figure 10:  $L_\infty$ -norm of (a) velocity magnitude error and (b) density error from solving the Euler equations for isentropic convecting vortex using various EBC schemes with  $201 \times 101$  grid points. Convective velocity ( $u_0 = 0.8, v_0 = 0.4$ ) with initial vortex location  $(x_0, y_0) = (0, 0)$  is used to simulate a subsonic vortex traveling through the top-right corner of computational domain.

N	1 – 2 – 1				2 – 4 – 2				3 – 4 – 3			
	$\log_{10} \ \varepsilon_\rho\ _2$	Rate	$\log_{10} \ \varepsilon_\rho\ _\infty$	Rate	$\log_{10} \ \varepsilon_\rho\ _2$	Rate	$\log_{10} \ \varepsilon_\rho\ _\infty$	Rate	$\log_{10} \ \varepsilon_\rho\ _2$	Rate	$\log_{10} \ \varepsilon_\rho\ _\infty$	Rate
50	-2.97741		-1.99754		-3.55779		-2.68874		-3.0783		-2.14384	
100	-3.5008	1.714	-2.50662	1.667	-4.34167	2.566	-3.46567	2.544	-4.06836	3.242	-3.14236	3.269
150	-3.85544	1.997	-2.86293	2.007	-4.83949	2.804	-3.99159	2.962	-4.70384	3.579	-3.73467	3.336
200	-4.10382	1.977	-3.11973	2.043	-5.21171	2.962	-4.38812	3.155	-5.22411	4.140	-4.22631	3.912
250	-4.29947	2.010	-3.32405	2.099	-5.50531	3.016	-4.70008	3.204	-5.65743	4.451	-4.64963	4.349
N	3 – 6 – 3 (A)				3 – 6 – 3 (B)				4 – 6 – 4 (B)			
	$\log_{10} \ \varepsilon_\rho\ _2$	Rate	$\log_{10} \ \varepsilon_\rho\ _\infty$	Rate	$\log_{10} \ \varepsilon_\rho\ _2$	Rate	$\log_{10} \ \varepsilon_\rho\ _\infty$	Rate	$\log_{10} \ \varepsilon_\rho\ _2$	Rate	$\log_{10} \ \varepsilon_\rho\ _\infty$	Rate
50	-3.27896		-2.67444		-3.19404		-2.28162		-3.52224		-2.92804	
100	-4.3226	3.417	-3.67187	3.266	-4.25752	3.482	-3.32069	3.402	-4.65438	3.707	-4.04166	3.646
150	-5.0798	4.265	-4.24271	3.215	-4.94213	3.856	-3.97785	3.701	-5.47907	4.645	-4.82533	4.414
200	-5.6334	4.405	-4.73597	3.925	-5.50794	4.502	-4.51338	4.262	-6.06421	4.656	-5.38228	4.432
250	-6.04597	4.238	-5.1277	4.024	-5.96407	4.686	-4.95957	4.584	-6.52601	4.744	-5.83103	4.610
N	5 – 6 – 5 (B)											
	$\log_{10} \ \varepsilon\ _2$	Rate	$\log_{10} \ \varepsilon\ _\infty$	Rate								
50	-3.54629		-2.91818									
100	-5.37231	5.978	-4.33566	4.641								
150	-6.39434	5.756	-5.39133	5.946								
200	-7.13436	5.889	-6.12412	5.831								
250	-7.71226	5.937	-6.70115	5.928								

Table 5:  $L_2$ – and  $L_\infty$ –norm of the density error and convergence rates from solving the Euler equations for isentropic vortex convection on a  $N \times N$  grid using various schemes. Error calculations performed at  $t = 1.0$ .

## 5.2. Acoustic scatter by a rigid cylinder

This section examines the performance of the EBC schemes on curvilinear grid to solve problems where the exact (or target) values of all conservative variables are not known at the boundary, as is often the case in practical flow simulations. The strong BC implementations, unlike the weak enforcement, does not require target values for all conservative variables.

### 5.2.1. Initial pressure pulse

The Euler equations (66) are solved for scattering of an initial pressure pulse by a cylinder [34], as shown in Figure 11. The initial condition is given by

$$p = \frac{1}{\gamma} + \varepsilon \exp \left[ -(\ln 2) \frac{(x-4)^2 + y^2}{0.2^2} \right], \quad \rho = \left( 1 - \frac{1}{\gamma} \right) + p, \quad u = v = 0, \quad (75)$$

where a small value of  $\varepsilon = 10^{-4}$  is considered to trigger a linear response allowing comparison with the linearized Euler equations solution. The pressure disturbance is centered at  $(x_s, y_s) = (4, 0)$ . All quantities in (75) are non-dimensional, obtained from the density scale  $= \rho_\infty^*$ , velocity scale  $= c_\infty^*$ , length scale  $= r_0$  (cylinder radius) and pressure scale  $= \rho_\infty^* c_\infty^{*2}$ , where  $*$  denotes the dimensional quantities, subscript  $\infty$  denotes the ambient values and  $c$  is the speed of sound.

Figure 11(a) shows the computational grid and the boundary conditions for the problem. The inviscid wall imposes the no-penetration condition normal to the wall and slip condition in the tangential direction. The no-penetration condition makes the contravariant velocity  $U$  in (67) zero and, therefore,  $(\mathbf{L}^*)_1 = (\mathbf{L}^*)_2 = 0$  in (71), based on the eigenvalue arrangement of the characteristic matrices of [31].  $(\mathbf{L}^*)_4$  corresponds to the outgoing wave, therefore,  $(\mathbf{L}^*)_4 = (\mathbf{L}_{\text{SBP}})_4$  and the incoming wave  $(\mathbf{L}^*)_3 = (\mathbf{L}_{\text{SBP}})_4 + (\mathbf{S}_C)_3 - (\mathbf{S}_C)_4$ , see

[32]. The outflow has three outgoing and one incoming wave.  $(\mathbf{L}^*)_{1,2,3}$  are the convection terms of outgoing waves, therefore,  $(\mathbf{L}^*)_{1,2,3} = (\mathbf{L}_{\text{SBP}})_{1,2,3}$  and  $(\mathbf{L}^*)_4$  is specified using a pressure relaxation term, as in [35].

Figures 11(b) to (d) show the pressure fluctuation contours at various times. The solution consists of the incident pulse and the pulse reflected by the cylinder. The exact solution of pressure fluctuation is given by (see [34])

$$p'(x, y, t) = \text{Re} \left\{ \int_0^\infty (A_i(x, y, \omega) + A_r(x, y, \omega)) \omega e^{-i\omega t} d\omega \right\}.$$

The contribution of the incident pulse is estimated from

$$A_i(x, y, \omega) = \frac{1}{2b} e^{-i\omega^2/2b} J_0(\omega r_s),$$

where  $r_s = \sqrt{(x-4)^2 + y^2}$  and  $J_0$  is the Bessel function of order zero. The reflected pulse contribution is calculated from

$$A_r(x, y, \omega) = \sum_{k=0}^{\infty} C_k(\omega) H_k^{(1)}(r\omega) \cos(k\theta),$$

where  $H_k^{(1)}$  is the Hankel function of the first kind of order  $k$ ,  $r = \sqrt{x^2 + y^2}$ ,  $\theta = \text{atan2}(y, x)$ , and

$$C_k(\omega) = \frac{\omega}{2b} e^{-i\omega^2/2b} \frac{\varepsilon_k}{\pi \omega H_k^{(1)}(\omega)} \int_0^\pi J_1(\omega r_{s0}) \frac{1 - 4 \cos \theta}{r_{s0}} \cos(k\theta) d\theta,$$

where  $r_{s0} = r_s|_{r=r_0=1} = \sqrt{(\cos \theta - 4)^2 + \sin^2 \theta}$ ,  $\varepsilon_0 = 1$  and  $\varepsilon_k = 2$  for  $k \neq 0$ .

A comparison of the exact solution with the numerical results from various schemes at different spatial locations is shown in Figure 12. The subfigures in the left column show the time history of pressure fluctuation and the right column shows the respective errors. The spatial locations span different regions of the domain;  $x = 2, y = 0$  (top subfigures) lies in between the cylinder and the acoustic source,  $x = 0, y = 5$  (middle subfigures) lies above the cylinder, and  $x = -5, y = 0$  (bottom figures) lies behind the cylinder with respect to the source. The polar grid shown in Figure 11(a) with an outer radius of 12 and 251 grid points uniformly distributed in the radial and azimuthal directions is used for all simulations. The two peaks in the top and the middle subfigure of Figure 12(a) correspond to the incident and the reflected pulse.

All EBC schemes, except the 4 – 6 – 4(A) and 5 – 6 – 5(A) schemes, are stable for this problem. The error plots show the significance of high-order schemes for acoustic (wave propagation) problems. The second-order scheme has poor dispersion properties and, as a result, highest error among all schemes. The error decreases with increase in order-of-accuracy of the interior scheme, as expected.

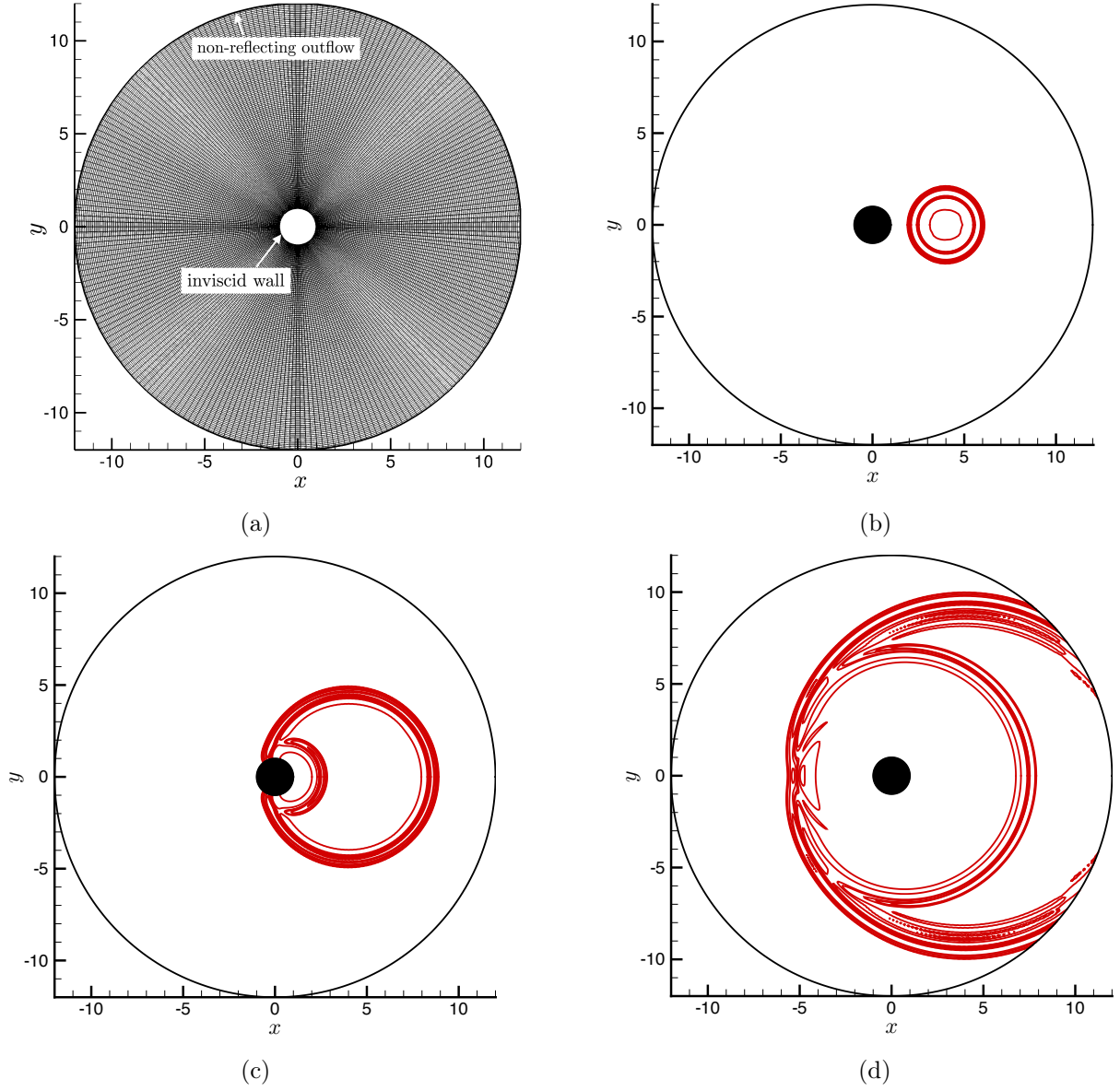


Figure 11: Initial pressure-pulse problem: (a) computational grid and boundary conditions, and pressure fluctuation contours at (b)  $t \approx 1.5$ , (c)  $t \approx 4.5$ , and (d)  $t \approx 9.5$ . The contour lines show 10 levels in the range  $[-5, 5] \times 10^{-6}$ .

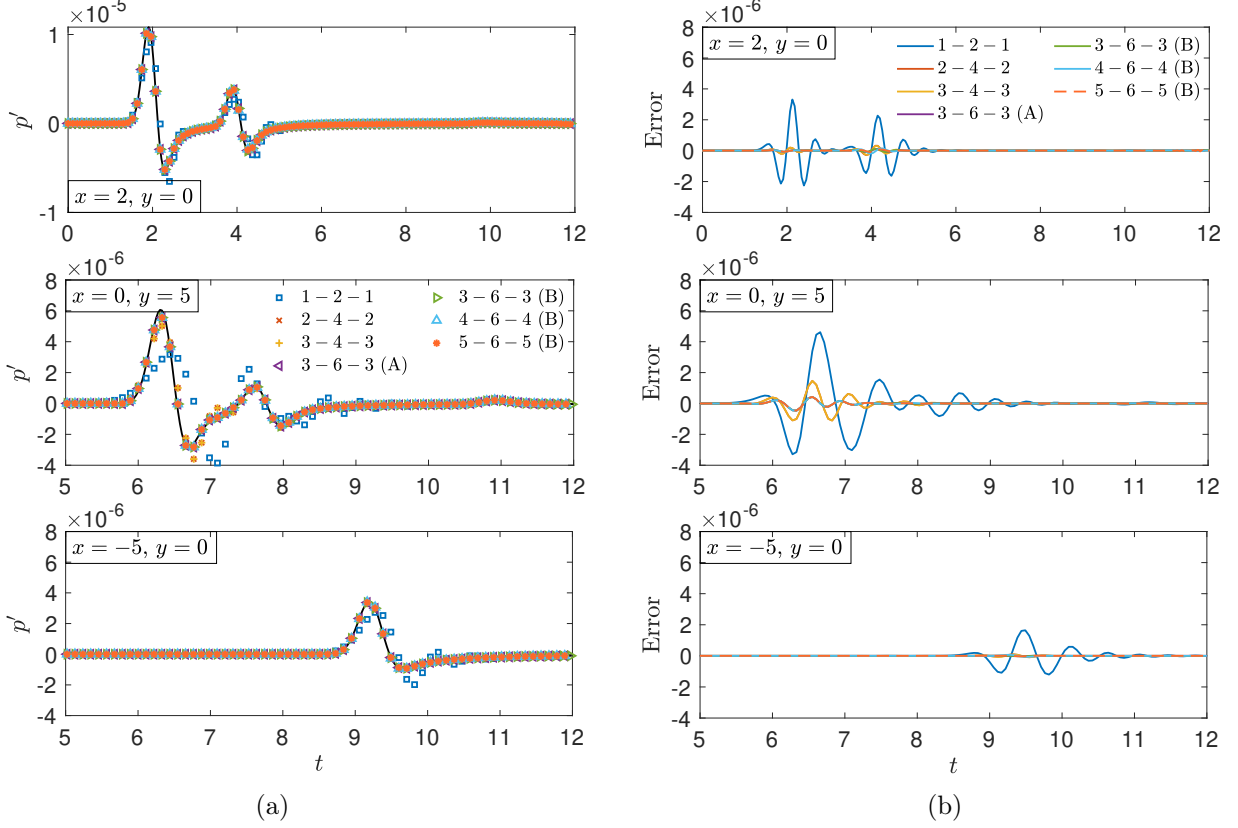


Figure 12: Numerical results from various schemes showing time history of (a) pressure fluctuation and (b) pressure-fluctuation error at  $x = 2, y = 0$  (top),  $x = 0, y = 5$  (middle) and  $x = -5, y = 0$  (bottom). The black solid line in subfigures of (a) shows the exact solution. Note the difference in axis scales of the top subfigure in each column. Legend is the same for each subfigure of a column. In subfigures of column (b), the absolute of the maximum error is less than  $1.5 \times 10^{-6}$  for the 2-4-2 and 3-4-3 schemes, and less than  $4.5 \times 10^{-7}$  for the 3-6-3, 4-6-4 (B) and 5-6-5 (B) schemes at all times.

### 5.2.2. Time-periodic pressure pulse

This section examines scheme performance for a series of pressure pulses scattered by a cylinder. The Euler equations are solved with the following source term in the right-hand side of (66):

$$S = \begin{bmatrix} 0 & 0 & 0 & \frac{1}{4} e^{-\ln 2 \left( \frac{(x-4)^2 + y^2}{(0.2)^2} \right)} \sin \omega t \end{bmatrix}^T. \quad (76)$$

The same computational grid and boundary conditions as used in the previous section and shown in 11(a) is used. The acoustic source is located at  $(x_s, y_s) = (4, 0)$  and the solution of the resulting scattering problem, governed by the linearized Euler equations, is discussed in [19, 36].

Figure 13 shows the pressure fluctuation contours at two times in the simulation. The pressure fluctuation at any point is a superposition of the incident and the reflected waves and Figure 14(a) shows the time evolution of the pressure fluctuation at the same spatial locations chosen in Figure 12 and Figure 14(b) shows the pressure fluctuation errors at those locations. All EBC schemes, except the 4-6-4 (A) and 5-6-5 (A) schemes, are stable for this problem with the boundary condition implementations as described in the previous section. The high-order schemes show better performance, as expected.



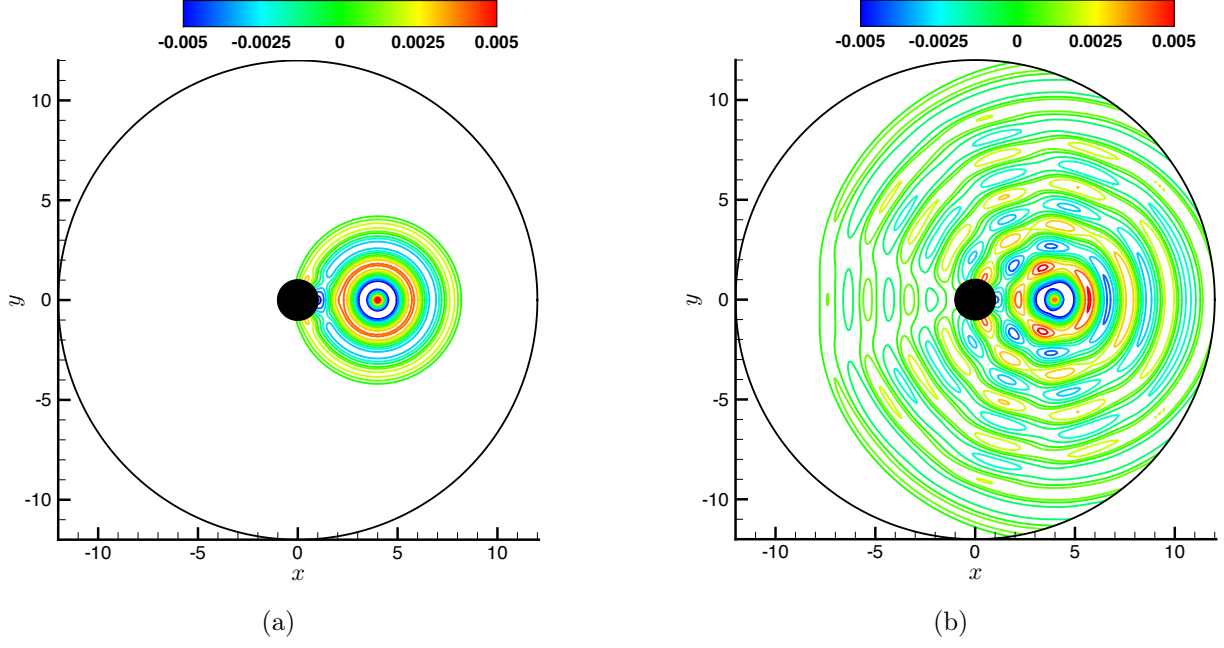


Figure 13: Pressure fluctuation contours for the time-periodic pressure-pulse problem at (a)  $t \approx 4$ , (b)  $t \approx 12$ .

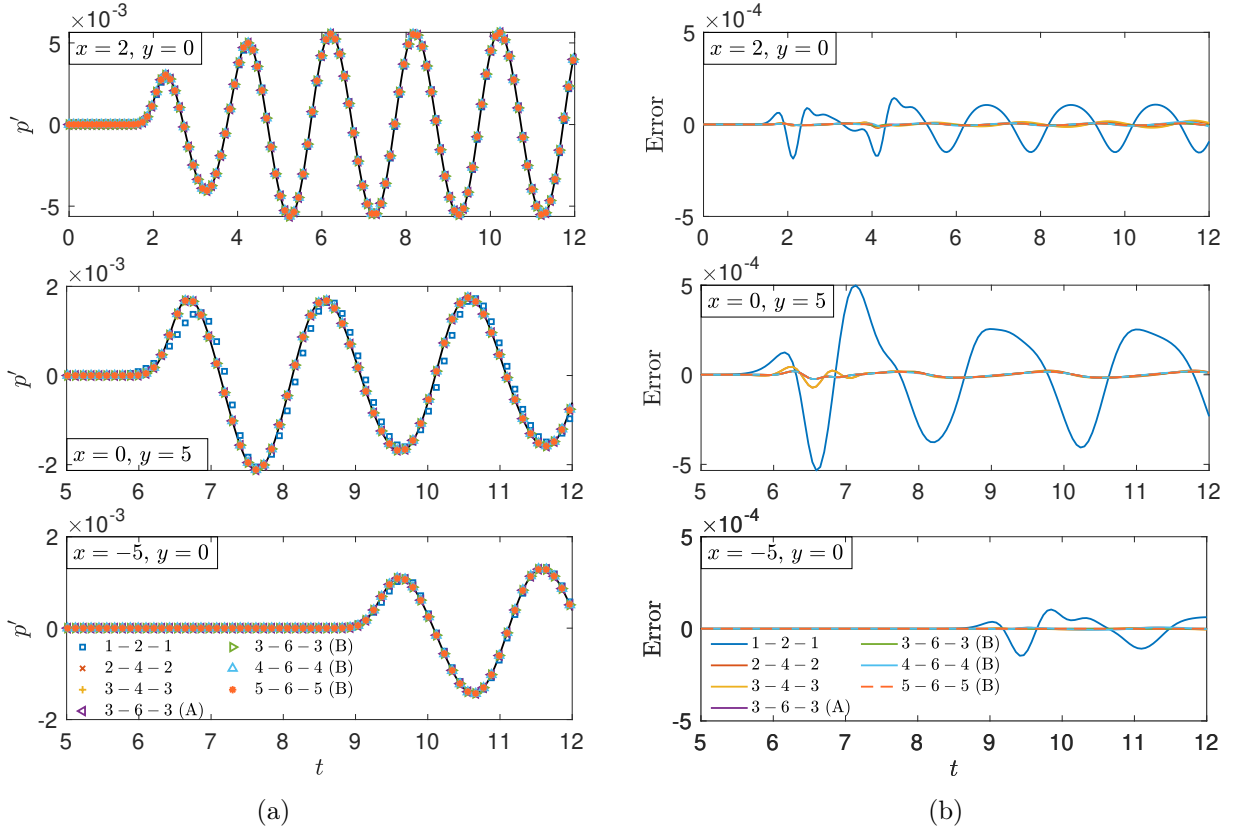


Figure 14: Numerical results from various schemes showing time history of (a) pressure fluctuation and (b) pressure-fluctuation error at  $x = 2, y = 0$  (top),  $x = 0, y = 5$  (middle) and  $x = -5, y = 0$  (bottom). The black solid line in subfigures of (a) shows the exact solution. Note the difference in axis scales of the top subfigure in each column. Legend is the same for each subfigure of a column. In subfigures of column (b), the absolute of the maximum error is less than  $7.5 \times 10^{-5}$  for the 2-4-2 and 3-4-3 schemes, and less than  $2.5 \times 10^{-5}$  for the 3-6-3, 4-6-4 (B) and 5-6-5 (B) schemes at all times.

## 6. Conclusions

A systematic approach is developed to derive time-stable high-order finite-difference schemes that enforce boundary conditions strongly for hyperbolic systems. Time-stability and conservation constraints are derived for non-square first-derivative operators that, by construction, exclude calculations at grid points where physical boundary condition is imposed. Schemes of global order-of-accuracy up to sixth-order are derived that show time-stability for problems that previously could not be solved for long times with high-order schemes and strong boundary conditions without additional stability measures, *e.g.* artificial dissipation/filters. The robustness of the proposed method is verified for various problems solving: (a) 1-D scalar advection equation, (b) 1-D coupled hyperbolic system, (c) 1-D inviscid Burgers' equation, (d) 2-D variable-coefficient advection equation, and (e) 2-D Euler equations in curvilinear coordinates. From among the various schemes derived in Section 3, the  $1-2-1$ ,  $2-4-2$ ,  $3-4-3$ ,  $3-6-3$  (B),  $4-6-4$  (B) and  $5-6-5$  (B) schemes are stable for all the test problems considered. The diagonal-norm  $3-6-3$  (A) scheme is stable for all problems, except the coupled system of Section 4.2. The  $4-6-4$  (A) and  $5-6-5$  (A) schemes are stable only for the scalar advection problem.

## Acknowledgements

This work was supported by the US Department of Energy through the Los Alamos National Laboratory. Los Alamos National Laboratory is operated by Triad National Security, LLC, for the National Nuclear Security Administration of U.S. Department of Energy (Contract No. 89233218CNA000001). Research presented in this article was supported by the Laboratory Directed Research and Development program of Los Alamos National Laboratory under project number 20190227ER. Computational resources were provided by the LANL Institutional Computing (IC) Program. Discussions with Dr. Harsha Nagarajan on optimization problems and tools is gratefully acknowledged.

## Appendix A. Additional proofs

**Lemma 1.** *The rows of a derivative operator  $D$  sum to zero, and hence the rows of  $Q = HD$  should also sum to zero.*

*Proof.* The rows of a derivative operator  $D$  sum to zero, *i.e.*,

$$\sum_{j=0}^n d_{ij} = 0, \quad 1 \leq i \leq n, \quad (\text{A.1})$$

where  $D$  is the non-square operator, as described in Section 2.1. The entries of  $Q$  are given by

$$q_{ij} = \sum_{k=1}^n h_{ik} d_{kj}, \quad 1 \leq i \leq n, \quad 0 \leq j \leq n, \quad (\text{A.2})$$

and the sum of the entries of  $i$ -th row of  $Q$  is

$$\sum_{j=0}^n q_{ij} = \sum_{j=0}^n \sum_{k=1}^n h_{ik} d_{kj} = \sum_{k=1}^n h_{ik} \left( \sum_{j=0}^n d_{kj} \right) = 0, \quad 1 \leq i \leq n, \quad (\text{A.3})$$

where the last equality follows from (A.1).  $\square$

**Lemma 2.** *A square  $(n+1) \times (n+1)$  derivative operator,  $\hat{D}$ , that ensures conservation when applied to a grid function that includes the boundary points, for solving (1), may not be conservative on row omission for enforcement of strong BC.*

*Proof.* Consider the grid function  $\mathbf{u}(t) = [u_0(t) \ \cdots \ u_n(t)]^T$  over a domain with  $n + 1$  equidistant grid points, as in Section 2.1. A square  $(n + 1) \times (n + 1)$  derivative operator,  $\hat{D}$ , typically satisfies the discrete conservation condition for (1) given by

$$\frac{dS}{dt} \approx \sum_{i=0}^n \left( \frac{d}{dt} \hat{H} \mathbf{u} \right)_i = - \sum_{i=0}^n \left( \hat{H} \hat{D} \mathbf{u} \right)_i = u_0(t) - u_n(t), \quad (\text{A.4})$$

where  $\hat{H}$  is a  $(n+1) \times (n+1)$  matrix that constitutes a quadrature for the domain and  $S = \int_0^1 U dx$ , as in Section 2.1. (A.4) implies for the entries  $\hat{q}_{ij}$  of  $\hat{Q} = \hat{H}\hat{D}$  that

$$\sum_{i=0}^n \hat{q}_{ij} = \sum_{i=0}^n \sum_{k=0}^n \hat{h}_{ik} \hat{d}_{kj} = \begin{cases} -1 & j=0 \\ 1 & j=n \\ 0 & \text{otherwise} \end{cases}, \quad (\text{A.5})$$

where  $\hat{h}_{ik}$  and  $\hat{d}_{kj}$  denote the entries of  $\hat{H}$  and  $\hat{D}$ , respectively.

To enforce BC strongly, if the first row of  $\hat{D}$  is omitted, *i.e.*  $\hat{d}_{kj} = 0$  is substituted for  $k = 0$ , then (A.5) may not hold unless  $\hat{d}_{0j} = 0$  for all  $0 \leq j \leq n$ . If  $\hat{D}$  is a valid derivative operator at all grid points, including the boundary points, then  $\hat{d}_{0j} \neq 0$  for some values of  $j$ . The omission of the first row of  $\hat{D}$ , therefore, introduces a conservation error at the  $j$ -th grid point of  $\sum_{i=0}^n \hat{h}_{i0} \hat{d}_{0j}$ , which is  $\mathcal{O}(1)$ .

## Appendix B. High-order stencils

### Appendix B.1. 2 – 4 – 2 stencil

$$D = \frac{1}{\Delta x} \begin{bmatrix} d_{10} & d_{11} & d_{12} & d_{13} & d_{14} & d_{15} & d_{16} & & & & & & & & & & & & & \\ d_{20} & d_{21} & d_{22} & d_{23} & d_{24} & d_{25} & d_{26} & & & & & & & & & & & & & \\ d_{30} & d_{31} & d_{32} & d_{33} & d_{34} & d_{35} & d_{36} & & & & & & & & & & & & & \\ d_{40} & d_{41} & d_{42} & d_{43} & d_{44} & d_{45} & d_{46} & & & & & & & & & & & & & \\ & & & \frac{1}{12} & -\frac{2}{3} & 0 & \frac{2}{3} & -\frac{1}{12} & & & & & & & & & & & & \\ & & & & \ddots & \ddots & \ddots & \ddots & \ddots & & & & & & & & & & & \\ & & & & & \ddots & \ddots & \ddots & \ddots & \ddots & & & & & & & & & & \\ & & & & & & \frac{1}{12} & -\frac{2}{3} & 0 & \frac{2}{3} & -\frac{1}{12} & & & & & & & & & \\ & & & & & & & \frac{4}{49} & -\frac{32}{49} & 0 & \frac{59}{98} & 0 & -\frac{3}{98} & & & & & & & \\ & & & & & & & 0 & \frac{4}{43} & -\frac{59}{86} & 0 & \frac{59}{86} & -\frac{4}{43} & & & & & & \\ & & & & & & & 0 & 0 & 0 & -\frac{1}{2} & 0 & \frac{1}{2} & & & & & & \\ & & & & & & & 0 & 0 & \frac{3}{34} & \frac{4}{17} & -\frac{59}{34} & \frac{24}{17} & & & & & & \end{bmatrix}. \quad (\text{B.1})$$

$h_{11} = 1.117853598033634$	$h_{22} = 1.734954607723689$	$h_{33} = 0.493492831348563$	$h_{44} = 1.153698962894113$
$d_{10} = -0.558055563977424$	$d_{20} = -0.177806646597481$	$d_{30} = 0.197577181565075$	$d_{40} = 0.053103321910167$
$d_{11} = 0.206193447640676$	$d_{21} = -0.148032843241780$	$d_{31} = -0.349146497048670$	$d_{41} = 0.031031686127352$
$d_{12} = 0.229753040942520$	$d_{22} = 0.010938409310223$	$d_{32} = -0.469159274307636$	$d_{42} = -0.272872172147738$
$d_{13} = 0.154135831102631$	$d_{23} = 0.133448297494816$	$d_{33} = 0.026584989564182$	$d_{43} = -0.326375382961636$
$d_{14} = -0.032026755708402$	$d_{24} = 0.181452783034222$	$d_{34} = 0.763007924163851$	$d_{44} = 0.009492491845307$
$d_{15} = 0$	$d_{25} = 0$	$d_{35} = -0.168864323936802$	$d_{45} = 0.577851491687484$
$d_{16} = 0$	$d_{26} = 0$	$d_{36} = 0$	$d_{46} = -0.072231436460936$

Appendix B.2. 3-4-3 stencil

$$H = \Delta x \begin{bmatrix} h_{11} & \cdots & \cdots & h_{1\kappa} & & & & \\ \vdots & \ddots & & \ddots & \vdots & & & \\ \vdots & \ddots & \ddots & \vdots & & & & \\ h_{\kappa 1} & \cdots & \cdots & h_{\kappa\kappa} & & & & \\ & & & & 1 & & & \\ & & & & & \ddots & & \\ & & & & & & 1 & \\ & & & & & & & h_{n-\kappa+1, n-\kappa+1} & \cdots & \cdots & h_{n-\kappa+1, n} \\ & & & & & & & \vdots & \ddots & \ddots & \vdots \\ & & & & & & & \vdots & \ddots & \ddots & \vdots \\ & & & & & & & h_{n, n-\kappa} & \cdots & \cdots & h_{n, n} \end{bmatrix}, \quad (\text{B.2})$$

$$D = \frac{1}{\Delta x} \begin{bmatrix} d_{10} & d_{11} & d_{12} & d_{13} & d_{14} & d_{15} & d_{16} & & & & & & & & & \\ d_{20} & d_{21} & d_{22} & d_{23} & d_{24} & d_{25} & d_{26} & & & & & & & & & \\ d_{30} & d_{31} & d_{32} & d_{33} & d_{34} & d_{35} & d_{36} & & & & & & & & & \\ d_{40} & d_{41} & d_{42} & d_{43} & d_{44} & d_{45} & d_{46} & & & & & & & & & \\ & & & \frac{1}{12} & -\frac{2}{3} & 0 & \frac{2}{3} & -\frac{1}{12} & & & & & & & & \\ & & & & \ddots & \ddots & \ddots & \ddots & & & & & & & & \\ & & & & & \ddots & \ddots & \ddots & & & & & & & & \\ & & & & & & \ddots & \ddots & & & & & & & & \\ & & & & & & & \frac{1}{12} & -\frac{2}{3} & 0 & \frac{2}{3} & -\frac{1}{12} & & & & \\ & & & & & & & d_{n-3, n-5} & d_{n-3, n-4} & d_{n-3, n-3} & d_{n-3, n-2} & d_{n-3, n-1} & d_{n-3, n} \\ & & & & & & & d_{n-2, n-5} & d_{n-2, n-4} & d_{n-2, n-3} & d_{n-2, n-2} & d_{n-2, n-1} & d_{n-2, n} \\ & & & & & & & d_{n-1, n-5} & d_{n-1, n-4} & d_{n-1, n-3} & d_{n-1, n-2} & d_{n-1, n-1} & d_{n-1, n} \\ & & & & & & & d_{n, n-5} & d_{n, n-4} & d_{n, n-3} & d_{n, n-2} & d_{n, n-1} & d_{n, n} \end{bmatrix}. \quad (\text{B.3})$$

$$\begin{aligned} h_{11} &= 2.662623411481001 & h_{21} &= -3.662857334606219 & h_{31} &= 4.845452750771308 & h_{41} &= -0.577741641722005 \\ h_{12} &= -3.662857334606219 & h_{22} &= 11.599859702563682 & h_{32} &= -14.225114399799256 & h_{42} &= 2.495952305453010 \\ h_{13} &= 4.845452750771308 & h_{23} &= -14.225114399799256 & h_{33} &= 18.748062983315343 & h_{43} &= -4.140606875653522 \\ h_{14} &= -0.577741641722005 & h_{24} &= 2.495952305453010 & h_{34} &= -4.140606875653522 & h_{44} &= 2.019284293753345 \end{aligned}$$

$$\begin{aligned} h_{n-3, n-3} &= 0.991547920021318 & h_{n-2, n-3} &= 0.024489711272366 & h_{n-1, n-3} &= 0.025569685989836 & h_{n, n-3} &= 0.034781571605365 \\ h_{n-3, n-2} &= 0.024489711272366 & h_{n-2, n-2} &= 0.921604250242240 & h_{n-1, n-2} &= -0.085089573430309 & h_{n, n-2} &= -0.131837721417554 \\ h_{n-3, n-1} &= 0.025569685989836 & h_{n-2, n-1} &= -0.085089573430309 & h_{n-1, n-1} &= 1.282715361353326 & h_{n, n-1} &= 0.172637859420519 \\ h_{n-3, n} &= 0.034781571605365 & h_{n-2, n} &= -0.131837721417554 & h_{n-1, n} &= 0.172637859420519 & h_{n, n} &= 0.223029401502785 \end{aligned}$$

$$\begin{aligned} d_{10} &= -0.690403955121951 & d_{20} &= 0.096301007387885 & d_{30} &= 0.351829869235339 & d_{40} &= 0.466243313628903 \\ d_{11} &= 0.720229785844440 & d_{21} &= -0.290789707647730 & d_{31} &= -0.728121899285697 & d_{41} &= -1.570517872896785 \\ d_{12} &= -0.237335922326079 & d_{22} &= -1.797881076077462 & d_{32} &= -1.128035183932539 & d_{42} &= 1.582135154379611 \\ d_{13} &= -0.278208400034439 & d_{23} &= 3.840067899696216 & d_{33} &= 2.923429010547118 & d_{43} &= -0.281561494461919 \\ d_{14} &= 0.912402202444629 & d_{24} &= -2.769535276964783 & d_{34} &= -2.498304973719164 & d_{44} &= -1.436597418357559 \\ d_{15} &= -0.499560713972126 & d_{25} &= 1.086533653062125 & d_{35} &= 1.268093932543600 & d_{45} &= 1.444468185292948 \\ d_{16} &= 0.072877003165526 & d_{26} &= -0.164696499456251 & d_{36} &= -0.188890755388658 & d_{46} &= -0.204169867585201 \end{aligned}$$

$$\begin{aligned} d_{n-3, n-5} &= 0.084712992534149 & d_{n-2, n-5} &= -0.004526801776437 & d_{n-1, n-5} &= 0.000166583823251 & d_{n, n-5} &= -0.016015883556691 \\ d_{n-3, n-4} &= -0.682230742049626 & d_{n-2, n-4} &= 0.135260194481088 & d_{n-1, n-4} &= -0.002799925684066 & d_{n, n-4} &= 0.188516967200137 \\ d_{n-3, n-3} &= 0.048459708099516 & d_{n-2, n-3} &= -0.829106093892077 & d_{n-1, n-3} &= 0.176200531099212 & d_{n, n-3} &= -0.927242367855843 \\ d_{n-3, n-2} &= 0.600875402145022 & d_{n-2, n-2} &= 0.221025130674176 & d_{n-1, n-2} &= -1.013467878066627 & d_{n, n-2} &= 2.310784134758679 \\ d_{n-3, n-1} &= -0.041771920582776 & d_{n-2, n-1} &= 0.526861250773015 & d_{n-1, n-1} &= 0.508700945622487 & d_{n, n-1} &= -3.513829620032445 \\ d_{n-3, n} &= -0.010045438351831 & d_{n-2, n} &= -0.049513679519196 & d_{n-1, n} &= 0.331199743141655 & d_{n, n} &= 1.957786768656585 \end{aligned}$$

### Appendix B.3. 3 – 6 – 3 stencils

#### Appendix B.3.1. 3 – 6 – 3 (A) stencil

$$H = \Delta x \text{diag} \left( h_{11}, h_{22}, h_{33}, h_{44}, h_{55}, h_{66}, 1, \dots, 1, \frac{43801}{43200}, \frac{7877}{8640}, \frac{5359}{4320}, \frac{2711}{4320}, \frac{12013}{8640}, \frac{13649}{43200} \right),$$

$$D = \frac{1}{\Delta x} \begin{bmatrix} d_{10} & d_{11} & d_{12} & d_{13} & d_{14} & d_{15} & d_{16} & d_{17} & d_{18} & d_{19} \\ d_{20} & d_{21} & d_{22} & d_{23} & d_{24} & d_{25} & d_{26} & d_{27} & d_{28} & d_{29} \\ d_{30} & d_{31} & d_{32} & d_{33} & d_{34} & d_{35} & d_{36} & d_{37} & d_{38} & d_{39} \\ d_{40} & d_{41} & d_{42} & d_{43} & d_{44} & d_{45} & d_{46} & d_{47} & d_{48} & d_{49} \\ d_{50} & d_{51} & d_{52} & d_{53} & d_{54} & d_{55} & d_{56} & d_{57} & d_{58} & d_{59} \\ d_{60} & d_{61} & d_{62} & d_{63} & d_{64} & d_{65} & d_{66} & d_{67} & d_{68} & d_{69} \\ & & & & -\frac{1}{60} & \frac{3}{20} & -\frac{3}{4} & 0 & \frac{3}{4} & -\frac{3}{20} & \frac{1}{60} \\ & & & & & \ddots & \ddots & \ddots & \ddots & \ddots & \ddots \\ & & & & & & -\frac{1}{60} & \frac{3}{20} & -\frac{3}{4} & 0 & \frac{3}{4} & -\frac{3}{20} & \frac{1}{60} \\ & & & & & & & -\frac{720}{43801} & \frac{6480}{43801} & -\frac{32400}{43801} & 0 & \frac{342523}{525612} & \frac{25427}{262806} & -\frac{21999}{87602} & \frac{36661}{262806} & -\frac{15025}{525612} \\ & & & & & & & -\frac{144}{7877} & \frac{1296}{7877} & -\frac{342523}{472620} & 0 & \frac{4147}{15754} & \frac{47262}{15754} & -\frac{4147}{15754} & \frac{41287}{15754} & -\frac{24337}{15754} \\ & & & & & & & & -\frac{72}{5359} & -\frac{25427}{321540} & -\frac{4147}{21436} & 0 & -\frac{485}{1398} & \frac{20229}{21436} & -\frac{33311}{107180} \\ & & & & & & & & & \frac{21999}{21999} & -\frac{41287}{41287} & \frac{11155}{11155} & 0 & -\frac{311}{311} & \frac{30443}{30443} \\ & & & & & & & & & \frac{54220}{54220} & -\frac{32532}{32532} & \frac{16266}{16266} & 0 & -\frac{311}{311} & \frac{30443}{30443} \\ & & & & & & & & & -\frac{36661}{360390} & \frac{24337}{24337} & -\frac{20229}{24026} & \frac{311}{72078} & 0 & \frac{104009}{240260} \\ & & & & & & & & & \frac{15025}{163788} & -\frac{16863}{27298} & \frac{33311}{27298} & -\frac{30443}{81894} & -\frac{104009}{54596} & \frac{21600}{13649} \end{bmatrix}.$$

$$\begin{aligned} h_{11} &= 1.569899624034763 & h_{22} &= 1.141706532981222 & h_{33} &= 0.420000007271351 & h_{44} &= 1.588165624499523 \\ h_{55} &= 0.731480683796968 & h_{66} &= 1.048747527416174 \end{aligned}$$

$$\begin{aligned} d_{10} &= -0.4992671810396931 & d_{20} &= -0.1233509277116018 & d_{30} &= 0.4432869024811746 & d_{40} &= 0.0225380373859439 \\ d_{11} &= 0.1304417662883768 & d_{21} &= -0.1704566526366988 & d_{31} &= -1.3147367558953225 & d_{41} &= 0.1130863754794943 \\ d_{12} &= 0.1239642783054266 & d_{22} &= 0.0156167192503039 & d_{32} &= 0.6094949380484006 & d_{42} &= -0.4556109486366097 \\ d_{13} &= 0.3517355113550370 & d_{23} &= -0.2242151297354362 & d_{33} &= 0.0103164238027623 & d_{43} &= -0.0820197537972236 \\ d_{14} &= -0.1144021511860695 & d_{24} &= 0.6337755157455880 & d_{34} &= 0.3101451220368827 & d_{44} &= 0.0002963501237265 \\ d_{15} &= 0.0211349098815782 & d_{25} &= -0.0649836898329329 & d_{35} &= -0.1752569030861041 & d_{45} &= 0.3777445414810139 \\ d_{16} &= -0.0136071336046604 & d_{26} &= -0.0663858350792125 & d_{36} &= 0.1167502726122043 & d_{46} &= 0.0134711104601582 \\ d_{17} &= 0 & d_{27} &= 0 & d_{37} &= 0 & d_{47} &= 0.0104942875034956 \\ d_{18} &= 0 & d_{28} &= 0 & d_{38} &= 0 & d_{48} &= 0 \\ d_{19} &= 0 & d_{29} &= 0 & d_{39} &= 0 & d_{49} &= 0 \\ \\ d_{50} &= -0.000000087979982 & d_{60} &= -0.0238699791784202 \\ d_{51} &= -0.0453596216715787 & d_{61} &= 0.0203689003994859 \\ d_{52} &= 0.1014275631098934 & d_{62} &= 0.0722701504661322 \\ d_{53} &= 0.1006286320350039 & d_{63} &= -0.0467558817200428 \\ d_{54} &= -0.8201459162372032 & d_{64} &= -0.0203999094132494 \\ d_{55} &= 0.000000002607273 & d_{65} &= -0.5898785954822714 \\ d_{56} &= 0.8457280310897003 & d_{66} &= 0.0002623394305700 \\ d_{57} &= -0.2050635147621129 & d_{67} &= 0.7151387539838061 \\ d_{58} &= 0.0227848349735681 & d_{68} &= -0.1430277507967612 \\ d_{59} &= 0 & d_{69} &= 0.0158919723107512 \end{aligned}$$

### Appendix B.3.2. 3 – 6 – 3 (B) stencil

$$D = \frac{1}{\Delta x} \begin{bmatrix} d_{10} & \cdots & \cdots & \cdots & \cdots & \cdots & \cdots & d_{1,\kappa+3} \\ \vdots & \ddots & \ddots & \ddots & \ddots & \ddots & \ddots & \vdots \\ \vdots & \ddots & \ddots & \ddots & \ddots & \ddots & \ddots & \vdots \\ d_{\kappa 0} & \cdots & \cdots & \cdots & \cdots & \cdots & \cdots & d_{\kappa,\kappa+3} \\ & & -\frac{1}{60} & \frac{3}{20} & -\frac{3}{4} & 0 & \frac{3}{4} & -\frac{3}{20} & \frac{1}{60} \\ & & & \ddots & \ddots & \ddots & \ddots & \ddots & \ddots \\ & & & & -\frac{1}{60} & \frac{3}{20} & -\frac{3}{4} & 0 & \frac{3}{4} & -\frac{3}{20} & \frac{1}{60} \\ & & & & & d_{n-\kappa+1,n-\kappa-2} & \cdots & \cdots & \cdots & \cdots & d_{n-\kappa+1,n} \\ & & & & & \vdots & \ddots & \ddots & \ddots & \ddots & \vdots \\ & & & & & \vdots & \ddots & \ddots & \ddots & \ddots & \vdots \\ & & & & & d_{n,n-\kappa-2} & \cdots & \cdots & \cdots & \cdots & d_{n,n} \end{bmatrix}. \quad (\text{B.4})$$

The entries of the norm matrix using  $\kappa = 4$  in (B.2) are given by

$$\begin{aligned} h_{11} &= 2.045837402052668 & h_{21} &= -1.422895779360524 & h_{31} &= 2.358103456201289 & h_{41} &= -0.407383114161261 \\ h_{12} &= -1.422895779360524 & h_{22} &= 4.189852738269392 & h_{32} &= -5.800817973799357 & h_{42} &= 1.164077862201690 \\ h_{13} &= 2.358103456201289 & h_{23} &= -5.800817973799357 & h_{33} &= 8.959999999686937 & h_{43} &= -2.008929521103727 \\ h_{14} &= -0.407383114161261 & h_{24} &= 1.164077862201690 & h_{34} &= -2.008929521103727 & h_{44} &= 1.540000000034780 \end{aligned}$$

$$\begin{aligned} h_{n-3,n-3} &= 1.010565909795035 & h_{n-2,n-3} &= -0.022159678607914 & h_{n-1,n-3} &= 0.049290321977698 & h_{n,n-3} &= -0.011307664275930 \\ h_{n-3,n-2} &= -0.022159678607914 & h_{n-2,n-2} &= 1.009529522678526 & h_{n-1,n-2} &= -0.066752758640902 & h_{n,n-2} &= -0.041450418763043 \\ h_{n-3,n-1} &= 0.049290321977698 & h_{n-2,n-1} &= -0.066752758640902 & h_{n-1,n-1} &= 1.103973967122970 & h_{n,n-1} &= 0.159321802873567 \\ h_{n-3,n} &= -0.011307664275930 & h_{n-2,n} &= -0.041450418763043 & h_{n-1,n} &= 0.159321802873567 & h_{n,n} &= 0.242047391276517 \end{aligned}$$

The entries of the derivative operator using  $\kappa = 4$  in (B.4) are given by

$$\begin{aligned} d_{10} &= -0.557228726233500 & d_{20} &= -0.038048498367394 & d_{30} &= 0.160087101995452 & d_{40} &= 0.096357281831583 \\ d_{11} &= 0.387405167342470 & d_{21} &= -0.178678093125937 & d_{31} &= -0.417645479698753 & d_{41} &= -0.444058853516611 \\ d_{12} &= -0.307586250304798 & d_{22} &= -0.737057589050130 & d_{32} &= -0.278300705588224 & d_{42} &= 0.906068656223521 \\ d_{13} &= 0.665755271886352 & d_{23} &= 1.168160792262199 & d_{33} &= 0.262248552082195 & d_{43} &= -1.427979677257400 \\ d_{14} &= -0.165589846507650 & d_{24} &= -0.230141306503343 & d_{34} &= 0.150540538354339 & d_{44} &= 0.326571019687846 \\ d_{15} &= -0.031173847980726 & d_{25} &= 0.031224919042442 & d_{35} &= 0.160747181902842 & d_{45} &= 0.664858326531560 \\ d_{16} &= 0.010197479042666 & d_{26} &= -0.020973095045625 & d_{36} &= -0.045343495032010 & d_{46} &= -0.138002135936081 \\ d_{17} &= -0.001779247244814 & d_{27} &= 0.005512870787788 & d_{37} &= 0.007666305984159 & d_{47} &= 0.016185382435582 \end{aligned}$$

$$\begin{aligned} d_{n-3,n-6} &= -0.016561684177261 & d_{n-2,n-6} &= -0.000361638454691 & d_{n-1,n-6} &= 0.000926155340965 & d_{n,n-6} &= -0.001445257338767 \\ d_{n-3,n-5} &= 0.148693519140655 & d_{n-2,n-5} &= -0.013405297064079 & d_{n-1,n-5} &= -0.008973007982595 & d_{n,n-5} &= 0.010557093852612 \\ d_{n-3,n-4} &= -0.741094886543546 & d_{n-2,n-4} &= 0.133029048031689 & d_{n-1,n-4} &= 0.030656091288366 & d_{n,n-4} &= -0.032019044358739 \\ d_{n-3,n-3} &= -0.024655295020487 & d_{n-2,n-3} &= -0.724163785725475 & d_{n-1,n-3} &= 0.115249274519848 & d_{n,n-3} &= -0.281922947649156 \\ d_{n-3,n-2} &= 0.782025275575096 & d_{n-2,n-2} &= 0.013794616447447 & d_{n-1,n-2} &= -0.953846621578270 & d_{n,n-2} &= 1.453991030655289 \\ d_{n-3,n-1} &= -0.169802610554259 & d_{n-2,n-1} &= 0.681982248203315 & d_{n-1,n-1} &= 0.478629162310713 & d_{n,n-1} &= -2.978250966158610 \\ d_{n-3,n} &= 0.021395681579801 & d_{n-2,n} &= -0.090875191438207 & d_{n-1,n} &= 0.337358946100972 & d_{n,n} &= 1.829090090997372 \end{aligned}$$

### Appendix B.4. 4 – 6 – 4 stencils

The entries of the bottom-right corner of the norm matrix and the derivative operator using  $\kappa = 5$  in (B.2) and (B.4), respectively, are given by

$$\begin{aligned}
h_{n-4,n-4} &= 0.994743173089164 & h_{n-3,n-4} &= 0.012702589663772 & h_{n-2,n-4} &= -0.014945113147020 & h_{n-1,n-4} &= 0.002437970776156 \\
h_{n-4,n-3} &= 0.012702589663772 & h_{n-3,n-3} &= 0.996688103543339 & h_{n-2,n-3} &= -0.033668929307689 & h_{n-1,n-3} &= 0.083738352246659 \\
h_{n-4,n-2} &= -0.014945113147020 & h_{n-3,n-2} &= -0.033668929307689 & h_{n-2,n-2} &= 1.135659889711249 & h_{n-1,n-2} &= -0.224293929307689 \\
h_{n-4,n-1} &= 0.002437970776156 & h_{n-3,n-1} &= 0.083738352246659 & h_{n-2,n-1} &= -0.224293929307689 & h_{n-1,n-1} &= 1.284805387493956 \\
h_{n-4,n} &= -0.025309939952137 & h_{n-3,n} &= 0.088414051023070 & h_{n-2,n} &= -0.165813168702575 & h_{n-1,n} &= 0.220630830404512
\end{aligned}$$

$$\begin{aligned}
& & d_{n-4,n-7} &= -0.016855969515846 & d_{n-3,n-7} &= 0.000451859001228 \\
h_{n,n-4} &= -0.025309939952137 & d_{n-4,n-6} &= 0.152155584643842 & d_{n-3,n-6} &= -0.021513276414185 \\
& & d_{n-4,n-5} &= -0.763189552243062 & d_{n-3,n-5} &= 0.178050404568210 \\
& & d_{n-4,n-4} &= 0.040239591278958 & d_{n-3,n-4} &= -0.833367941671272 \\
& & d_{n-4,n-3} &= 0.684451064159228 & d_{n-3,n-3} &= 0.134084850910356 \\
& & d_{n-4,n-2} &= -0.091253627545672 & d_{n-3,n-2} &= 0.630659158801440 \\
& & d_{n-4,n-1} &= -0.010798262538989 & d_{n-3,n-1} &= -0.094436481013399 \\
& & d_{n-4,n} &= 0.005251171761542 & d_{n-3,n} &= 0.006071425817622
\end{aligned}$$

$$\begin{aligned}
d_{n-2,n-7} &= -0.000604193018940 & d_{n-1,n-7} &= 0.000472227775386 & d_{n,n-7} &= -0.003349401269035 \\
d_{n-2,n-6} &= 0.006135578055224 & d_{n-1,n-6} &= -0.004463729414499 & d_{n,n-6} &= 0.038715042428764 \\
d_{n-2,n-5} &= -0.050238711716186 & d_{n-1,n-5} &= 0.022529389079660 & d_{n,n-5} &= -0.241412916288153 \\
d_{n-2,n-4} &= 0.263639976748788 & d_{n-1,n-4} &= -0.145552309652637 & d_{n,n-4} &= 0.993567989425527 \\
d_{n-2,n-3} &= -0.987070928608220 & d_{n-1,n-3} &= 0.596328630632108 & d_{n,n-3} &= -2.550547932312972 \\
d_{n-2,n-2} &= 0.302414425063164 & d_{n-1,n-2} &= -1.583926766842706 & d_{n,n-2} &= 4.093976813485549 \\
d_{n-2,n-1} &= 0.520433470085344 & d_{n-1,n-1} &= 0.871906717060636 & d_{n,n-1} &= -4.512361651982872 \\
d_{n-2,n} &= -0.054709616609174 & d_{n-1,n} &= 0.242705841362054 & d_{n,n} &= 2.181412056513190
\end{aligned}$$

#### Appendix B.4.1. 4 – 6 – 4 (A) stencil

The entries of the top-left corner of the norm matrix and the derivative operator using  $\kappa = 5$  in (B.2) and (B.4), respectively, are given by

$$\begin{aligned}
h_{11} &= 248.313472979432 & h_{21} &= -987.545180881491 & h_{31} &= 1483.762258933766 & h_{41} &= -988.120193457931 \\
h_{12} &= -987.545180881491 & h_{22} &= 3948.679193565772 & h_{32} &= -5930.183409878173 & h_{42} &= 3950.771260587214 \\
h_{13} &= 1483.762258933766 & h_{23} &= -5930.183409878173 & h_{33} &= 8907.758757559563 & h_{43} &= -5934.857485536984 \\
h_{14} &= -988.120193457931 & h_{24} &= 3950.771260587214 & h_{34} &= -5934.857485536984 & h_{44} &= 3957.03964543159 \\
h_{15} &= 246.498156799661 & h_{25} &= -985.970231796911 & h_{35} &= 1481.481123126835 & h_{45} &= -987.870787805899
\end{aligned}$$

$$\begin{aligned}
& & d_{10} &= -0.566760969598294 & d_{20} &= -0.0952114718509664 \\
& & d_{11} &= 0.694582109588709 & d_{21} &= 0.307521944126242 \\
h_{51} &= 246.498156799661 & d_{12} &= -1.37062913557195 & d_{22} &= -2.22020985169196 \\
h_{52} &= -985.970231796911 & d_{13} &= 2.01725539707268 & d_{23} &= 3.41035813328297 \\
h_{53} &= 1481.481123126835 & d_{14} &= -0.747279248823379 & d_{24} &= -2.0971079059257 \\
h_{54} &= -987.870787805899 & d_{15} &= -0.175947135410814 & d_{25} &= 0.92428837057582 \\
h_{55} &= 247.777910283461 & d_{16} &= 0.181482809422829 & d_{26} &= -0.282690848466388 \\
& & d_{17} &= -0.0364963995849044 & d_{27} &= 0.059454818567195 \\
& & d_{18} &= 0.00379257290479587 & d_{28} &= -0.00640318861617935
\end{aligned}$$

$d_{30} = 0.141070748551522$	$d_{40} = 0.146833651694254$	$d_{50} = -0.0734874370953696$
$d_{31} = -0.540318020783637$	$d_{41} = -0.846079417529063$	$d_{51} = 0.393755200786878$
$d_{32} = 0.308505050584258$	$d_{42} = 2.11776490026556$	$d_{52} = -0.888509050375232$
$d_{33} = -0.453275837811294$	$d_{43} = -3.29025952180062$	$d_{53} = 1.17542657060672$
$d_{34} = 0.258315092401369$	$d_{44} = 1.93591476658305$	$d_{54} = -1.43680852826521$
$d_{35} = 0.507232471985744$	$d_{45} = -0.1396000683557$	$d_{55} = 0.263680530967524$
$d_{36} = -0.269707874025708$	$d_{46} = 0.0957588402491774$	$d_{56} = 0.69196864839615$
$d_{37} = 0.0534670051094002$	$d_{47} = -0.0237816252075619$	$d_{57} = -0.142210236162081$
$d_{38} = -0.00528863601091192$	$d_{48} = 0.00344847410083534$	$d_{58} = 0.016184301140324$

#### Appendix B.4.2. 4 – 6 – 4 (B) stencil

The entries of the top-left corner of the derivative operator using  $\kappa = 5$  in (B.4) are given by

$d_{10} = 0.308742182657966$	$d_{20} = 0.918871513183198$	$d_{30} = 0.554442928817947$	$d_{40} = -0.0173506759950015$
$d_{11} = -3.615633042658463$	$d_{21} = -4.775555615408521$	$d_{31} = -2.618433465434184$	$d_{41} = 0.00499474840808696$
$d_{12} = 7.039700375168833$	$d_{22} = 8.001353830788842$	$d_{32} = 4.509386901259435$	$d_{42} = 0.317142561487607$
$d_{13} = -6.022751605387267$	$d_{23} = -6.949134956033721$	$d_{33} = -4.756465144522829$	$d_{43} = -1.303950001331169$
$d_{14} = 2.870122773071738$	$d_{24} = 3.298807934815511$	$d_{34} = 2.559021809995832$	$d_{44} = 0.719009376373294$
$d_{15} = -0.622721610912302$	$d_{25} = -0.376650326988763$	$d_{35} = -0.0961398768843027$	$d_{45} = 0.28409960616814$
$d_{16} = 0.0629514020595184$	$d_{26} = -0.133588974966265$	$d_{36} = -0.17916253576769$	$d_{46} = -0.00306427445737409$
$d_{17} = -0.0231794503975544$	$d_{27} = 0.017366189468941$	$d_{37} = 0.0301526047593198$	$d_{47} = -0.00147096824943352$
$d_{18} = 0.00276897639769214$	$d_{28} = -0.00146959485897978$	$d_{38} = -0.0028032222338317$	$d_{48} = 0.000589627595865209$

$d_{50} = -0.0334877852699657$
$d_{51} = 0.264020542031309$
$d_{52} = -0.859420860855764$
$d_{53} = 1.581629983796928$
$d_{54} = -2.163411008345286$
$d_{55} = 0.827025083216811$
$d_{56} = 0.467630480190381$
$d_{57} = -0.0945584425594451$
$d_{58} = 0.0105720077950345$

#### Appendix B.5. 5 – 6 – 5 stencils

The entries of the bottom-right corner of the norm matrix and the derivative operator using  $\kappa = 6$  in (B.2) and (B.4), respectively, are given by

$h_{n-5,n-5} = 0.997112154219008$	$h_{n-4,n-5} = 0.009012101689827$	$h_{n-3,n-5} = -0.022392149604879$	$h_{n-2,n-5} = 0.005215263365474$
$h_{n-5,n-4} = 0.009012101689827$	$h_{n-4,n-4} = 0.992126912920984$	$h_{n-3,n-4} = 0.024062858080948$	$h_{n-2,n-4} = 0.096006933828455$
$h_{n-5,n-3} = -0.022392149604879$	$h_{n-4,n-3} = 0.024062858080948$	$h_{n-3,n-3} = 0.933515071176799$	$h_{n-2,n-3} = -0.204355507710995$
$h_{n-5,n-2} = 0.005215263365474$	$h_{n-4,n-2} = 0.096006933828455$	$h_{n-3,n-2} = -0.204355507710995$	$h_{n-2,n-2} = 1.540305194633593$
$h_{n-5,n-1} = -0.008020444517406$	$h_{n-4,n-1} = -0.054924473113918$	$h_{n-3,n-1} = 0.168229156050676$	$h_{n-2,n-1} = -0.420381586363496$
$h_{n-5,n} = 0.015485111885013$	$h_{n-4,n} = -0.067094518591481$	$h_{n-3,n} = 0.166449831266709$	$h_{n-2,n} = -0.214244001456731$



$h_{n-1,n-5} = -0.008020444517406$	$h_{n,n-5} = 0.015485111885013$	$d_{n-5,n-8} = -0.016790219586135$	$d_{n-4,n-8} = 0.000335647706472$
$h_{n-1,n-4} = -0.054924473113918$	$h_{n,n-4} = -0.067094518591481$	$d_{n-5,n-7} = 0.151447623981688$	$d_{n-4,n-7} = -0.020437373269251$
$h_{n-1,n-3} = 0.168229156050676$	$h_{n,n-3} = 0.166449831266709$	$d_{n-5,n-6} = -0.759413964351020$	$d_{n-4,n-6} = 0.173771424580478$
$h_{n-1,n-2} = -0.420381586363496$	$h_{n,n-2} = -0.214244001456731$	$d_{n-5,n-5} = 0.033002645980902$	$d_{n-4,n-5} = -0.832239980391041$
$h_{n-1,n-1} = 1.372682468476539$	$h_{n,n-1} = 0.245308397986124$	$d_{n-5,n-4} = 0.684178100364496$	$d_{n-4,n-4} = 0.163107924885430$
$h_{n-1,n} = 0.245308397986124$	$h_{n,n} = 0.187544252984440$	$d_{n-5,n-3} = -0.072207450115457$	$d_{n-4,n-3} = 0.557718072287135$
		$d_{n-5,n-2} = -0.037537201587995$	$d_{n-4,n-2} = -0.016186628097697$
		$d_{n-5,n-1} = 0.020643297083249$	$d_{n-4,n-1} = -0.034264874502414$
		$d_{n-5,n} = -0.003322831769729$	$d_{n-4,n} = 0.008195786800888$
$d_{n-3,n-8} = -0.000833253616691$	$d_{n-2,n-8} = 0.000231829740432$	$d_{n-1,n-8} = -0.000470147387258$	$d_{n,n-8} = 0.003125730052250$
$d_{n-3,n-7} = 0.009417665140437$	$d_{n-2,n-7} = -0.001736492944214$	$d_{n-1,n-7} = 0.004920945349098$	$d_{n,n-7} = -0.036594938017142$
$d_{n-3,n-6} = -0.076293338363404$	$d_{n-2,n-6} = 0.006908602965455$	$d_{n-1,n-6} = -0.028508366561945$	$d_{n,n-6} = 0.237763628286536$
$d_{n-3,n-5} = 0.356651264765950$	$d_{n-2,n-5} = -0.051301064761743$	$d_{n-1,n-5} = 0.144038600727081$	$d_{n,n-5} = -1.033128954285273$
$d_{n-3,n-4} = -1.160146775125601$	$d_{n-2,n-4} = 0.280758783877498$	$d_{n-1,n-4} = -0.515223608649905$	$d_{n,n-4} = 2.911212074070740$
$d_{n-3,n-3} = 0.483651809397069$	$d_{n-2,n-3} = -1.033735092951674$	$d_{n-1,n-3} = 1.211437591702418$	$d_{n,n-3} = -5.296382704820362$
$d_{n-3,n-2} = 0.413372783672142$	$d_{n-2,n-2} = 0.356009297822054$	$d_{n-1,n-2} = -2.145907357537280$	$d_{n,n-2} = 6.367684045488291$
$d_{n-3,n-1} = -0.021867815731941$	$d_{n-2,n-1} = 0.491506066402955$	$d_{n-1,n-1} = 1.138568131957575$	$d_{n,n-1} = -5.520846545389325$
$d_{n-3,n} = -0.003952340137962$	$d_{n-2,n} = -0.048641930150763$	$d_{n-1,n} = 0.191144210400217$	$d_{n,n} = 2.367167664614281$

#### Appendix B.5.1. 5 – 6 – 5 (A) stencil

The entries of the top-left corner of the norm matrix and the derivative operator using  $\kappa = 6$  in (B.2) and (B.4), respectively, are given by

$h_{11} = 147.408285739017$	$h_{21} = -725.682919987077$	$h_{31} = 1451.61017011212$	$h_{41} = -1450.25210681305$
$h_{12} = -725.682919987077$	$h_{22} = 3622.24425362375$	$h_{32} = -7250.54501721347$	$h_{42} = 7251.35539237299$
$h_{13} = 1451.61017011212$	$h_{23} = -7250.54501721347$	$h_{33} = 14515.38089509317$	$h_{43} = -14518.46598574749$
$h_{14} = -1450.25210681305$	$h_{24} = 7251.35539237299$	$h_{34} = -14518.46598574749$	$h_{44} = 14527.95288849271$
$h_{15} = 723.339203731005$	$h_{25} = -3619.58557736239$	$h_{35} = 7248.95215697340$	$h_{45} = -7255.76536811803$
$h_{16} = -144.557498321676$	$h_{26} = 723.397016692929$	$h_{36} = -1448.64972741814$	$h_{46} = 1450.16997377150$
		$d_{10} = -0.494739531497564$	$d_{20} = 0.069732695901814$
		$d_{11} = 0.693200901376322$	$d_{21} = -0.568807045425389$
$h_{51} = 723.339203731005$	$h_{61} = -144.557498321676$	$d_{12} = -2.474628350485542$	$d_{22} = -0.362536107219290$
$h_{52} = -3619.58557736239$	$h_{62} = 723.397016692929$	$d_{13} = 5.045656072888681$	$d_{23} = 1.511686992564767$
$h_{53} = 7248.9521569734$	$h_{63} = -1448.64972741814$	$d_{14} = -4.322143918825208$	$d_{24} = -1.339988843377419$
$h_{54} = -7255.76536811803$	$h_{64} = 1450.16997377150$	$d_{15} = 1.934321973501119$	$d_{25} = 1.160243244128906$
$h_{55} = 3626.52436406343$	$h_{65} = -724.781040065685$	$d_{16} = -0.411441061134875$	$d_{26} = -0.623745886536177$
$h_{56} = -724.781040065685$	$h_{66} = 145.911967774039$	$d_{17} = 0.033182692880816$	$d_{27} = 0.163840211141727$
		$d_{18} = -0.003099913712388$	$d_{28} = -0.006978626929758$
		$d_{19} = -0.000308864994417$	$d_{29} = -0.003446634265830$

$d_{30} = 0.189524193114424$	$d_{40} = 0.082552107759926$	$d_{50} = -0.053574661922412$	$d_{60} = -0.041124980303590$
$d_{31} = -1.074862656554703$	$d_{41} = -0.560903026695448$	$d_{51} = 0.366177019090548$	$d_{61} = 0.226644773712233$
$d_{32} = 2.261220311751314$	$d_{42} = 1.696654263890278$	$d_{52} = -1.095199510948976$	$d_{62} = -0.490360879658560$
$d_{33} = -3.894124246008449$	$d_{43} = -3.224159124552080$	$d_{53} = 1.935367396541880$	$d_{63} = 0.468231756280699$
$d_{34} = 3.491379364042100$	$d_{44} = 2.440885789472983$	$d_{54} = -2.568520316220218$	$d_{64} = 0.027828125500143$
$d_{35} = -1.077406414839207$	$d_{45} = -0.779961690982964$	$d_{55} = 1.178756248689623$	$d_{65} = -0.933372825275117$
$d_{36} = 0.074549239986315$	$d_{46} = 0.454131233872320$	$d_{56} = 0.255838318888854$	$d_{66} = 0.182263392817766$
$d_{37} = 0.026517703404380$	$d_{47} = -0.125425255725840$	$d_{57} = -0.010439210103636$	$d_{67} = 0.683713273807763$
$d_{38} = 0.005432520553928$	$d_{48} = 0.016504770222655$	$d_{58} = -0.012111948123781$	$d_{68} = -0.139763799504671$
$d_{39} = -0.002230015457082$	$d_{49} = -0.000279067257728$	$d_{59} = 0.003706664114466$	$d_{69} = 0.015941162624349$

### Appendix B.5.2. 5 – 6 – 5 (B) stencil

The entries of the top-left corner of the derivative operator using  $\kappa = 6$  in (B.4) are given by

$d_{10} = -0.2372215319751228$	$d_{20} = 0.1907124386528013$	$d_{30} = 0.0590997222510325$	$d_{40} = -0.1405341238275227$
$d_{11} = -0.7722853927621035$	$d_{21} = -1.2015881189375732$	$d_{31} = -0.2318888245325529$	$d_{41} = 0.7898476503288872$
$d_{12} = 0.8879780463048134$	$d_{22} = 0.8766419901276702$	$d_{32} = -0.0723383565707714$	$d_{42} = -1.7316041416316885$
$d_{13} = 1.2286625272430147$	$d_{23} = 0.6003560614546122$	$d_{33} = -0.2856173677575855$	$d_{43} = 1.4719755191582560$
$d_{14} = -2.4149524456561413$	$d_{24} = -1.7024507711702204$	$d_{34} = 0.0720188647167593$	$d_{44} = -1.2756682901683880$
$d_{15} = 2.0988165544959010$	$d_{25} = 2.3225110015778299$	$d_{35} = 0.9916613863892865$	$d_{45} = 0.9061510331569869$
$d_{16} = -1.0569665797214214$	$d_{26} = -1.5193706978761616$	$d_{36} = -0.7545801862146135$	$d_{46} = 0.0387779927646424$
$d_{17} = 0.3140141361248970$	$d_{27} = 0.5115506200784167$	$d_{37} = 0.2622466833471242$	$d_{47} = -0.0690088400734462$
$d_{18} = -0.0521770805180847$	$d_{28} = -0.0851165930017976$	$d_{38} = -0.0442068786574461$	$d_{48} = 0.0108228083586796$
$d_{19} = 0.0041317664620954$	$d_{29} = 0.0067540690910218$	$d_{39} = 0.0036049570271975$	$d_{49} = -0.0007596080657851$
	$d_{50} = -0.1790974874602519$	$d_{60} = -0.0349891412307292$	
	$d_{51} = 1.0680475753500993$	$d_{61} = 0.0531878191820058$	
	$d_{52} = -2.6628124450495276$	$d_{62} = 0.4540380412859120$	
	$d_{53} = 3.6249194277126615$	$d_{63} = -1.9120500244629284$	
	$d_{54} = -3.2748360198473025$	$d_{64} = 3.4176152006529930$	
	$d_{55} = 0.9184440724400876$	$d_{65} = -3.8631726289977264$	
	$d_{56} = 0.6748223249297969$	$d_{66} = 1.7534442095653340$	
	$d_{57} = -0.1993238418264024$	$d_{67} = 0.1588527859071113$	
	$d_{58} = 0.0322518517588724$	$d_{68} = -0.0299901123893163$	
	$d_{59} = -0.0024154580065788$	$d_{69} = 0.0030638504869708$	

## References

- [1] M. M. Rai, P. Moin, Direct simulations of turbulent flow using finite-difference schemes, *Journal of Computational Physics* 96 (1) (1991) 15–53 (1991).
- [2] Y. Morinishi, T. S. Lund, O. V. Vasilyev, P. Moin, Fully conservative higher order finite difference schemes for incompressible flow, *Journal of Computational Physics* 143 (1) (1998) 90–124 (1998).
- [3] J. Ryu, D. Livescu, Turbulence structure behind the shock in canonical shock–vortical turbulence interaction, *Journal of Fluid Mechanics* 756 (2014).
- [4] N. Sharan, G. Matheou, P. E. Dimotakis, Turbulent shear-layer mixing: initial conditions, and direct-numerical and large-eddy simulations, *Journal of Fluid Mechanics* 877 (2019) 35–81 (2019).
- [5] C. K. Tam, Z. Dong, Wall boundary conditions for high-order finite-difference schemes in computational aeroacoustics, *Theoretical and Computational Fluid Dynamics* 6 (5-6) (1994) 303–322 (1994).
- [6] M. Zhuang, R. Chen, Optimized upwind dispersion-relation-preserving finite difference scheme for computational aeroacoustics, *AIAA Journal* 36 (11) (1998) 2146–2148 (1998).
- [7] T. Colonius, S. K. Lele, Computational aeroacoustics: progress on nonlinear problems of sound generation, *Progress in Aerospace Sciences* 40 (6) (2004) 345–416 (2004).

- [8] W. De Roeck, W. Desmet, M. Baelmans, P. Sas, An overview of high-order finite difference schemes for computational aeroacoustics, in: *Proceedings of the International Conference on Noise and Vibration Engineering*, Citeseer, 2004, pp. 353–368 (2004).
- [9] B. Gustafsson, *High order difference methods for time dependent PDE*, Vol. 38, Springer Science & Business Media, 2007 (2007).
- [10] L. N. Trefethen, Stability of finite-difference models containing two boundaries or interfaces, *Mathematics of Computation* 45 (172) (1985) 279–300 (1985).
- [11] M. H. Carpenter, D. Gottlieb, S. Abarbanel, Time-stable boundary conditions for finite-difference schemes solving hyperbolic systems: methodology and application to high-order compact schemes, *Journal of Computational Physics* 111 (2) (1994) 220–236 (1994).
- [12] P. Olsson, Summation by parts, projections, and stability. i, *Mathematics of Computation* 64 (211) (1995) 1035–1065 (1995).
- [13] P. Olsson, Summation by parts, projections, and stability. ii, *Mathematics of Computation* 64 (212) (1995) 1473–1493 (1995).
- [14] H.-O. Kreiss, G. Scherer, Finite element and finite difference methods for hyperbolic partial differential equations, in: *Mathematical aspects of finite elements in partial differential equations*, Elsevier, 1974, pp. 195–212 (1974).
- [15] H.-O. Kreiss, G. Scherer, On the existence of energy estimates for difference approximations for hyperbolic systems, Tech. rep., Technical report, Dept. of Scientific Computing, Uppsala University (1977).
- [16] B. Strand, Summation by parts for finite difference approximations for  $d/dx$ , *Journal of Computational Physics* 110 (1) (1994) 47–67 (1994).
- [17] D. C. D. R. Fernández, J. E. Hicken, D. W. Zingg, Review of summation-by-parts operators with simultaneous approximation terms for the numerical solution of partial differential equations, *Computers & Fluids* 95 (2014) 171–196 (2014).
- [18] N. Sharan, Time-stable high-order finite difference methods for overset grids, Ph.D. thesis, University of Illinois at Urbana-Champaign (2016).
- [19] N. Sharan, C. Pantano, D. J. Bodony, Time-stable overset grid method for hyperbolic problems using summation-by-parts operators, *Journal of Computational Physics* 361 (2018) 199–230 (2018).
- [20] P. T. Brady, D. Livescu, High-order, stable, and conservative boundary schemes for central and compact finite differences, *Computers & Fluids* 183 (2019) 84–101 (2019).
- [21] M. J. Corless, A. Frazho, *Linear systems and control: an operator perspective*, CRC Press, 2003 (2003).
- [22] S. S. Abarbanel, A. E. Chertock, A. Yefet, Strict stability of high-order compact implicit finite-difference schemes: the role of boundary conditions for hyperbolic PDEs, II, *Journal of Computational Physics* 160 (1) (2000) 67–87 (2000).
- [23] B. Gustafsson, The convergence rate for difference approximations to mixed initial boundary value problems, *Mathematics of Computation* 29 (130) (1975) 396–406 (1975).
- [24] B. Gustafsson, The convergence rate for difference approximations to general mixed initial-boundary value problems, *SIAM Journal on Numerical Analysis* 18 (2) (1981) 179–190 (1981).
- [25] A. Wächter, L. T. Biegler, On the implementation of an interior-point filter line-search algorithm for large-scale nonlinear programming, *Mathematical Programming* 106 (1) (2006) 25–57 (2006).
- [26] S. S. Abarbanel, A. E. Chertock, Strict stability of high-order compact implicit finite-difference schemes: the role of boundary conditions for hyperbolic PDEs, I, *Journal of Computational Physics* 160 (1) (2000) 42–66 (2000).
- [27] M. Svärd, On coordinate transformations for summation-by-parts operators, *J. Sci. Comput.* 20 (1) (2004) 29–42 (2004).
- [28] M. H. Carpenter, D. Gottlieb, S. Abarbanel, The stability of numerical boundary treatments for compact high-order finite-difference schemes, *Journal of Computational Physics* 108 (2) (1993) 272–295 (1993).
- [29] A. W. Cook, J. J. Riley, Direct numerical simulation of a turbulent reactive plume on a parallel computer, *Journal of Computational Physics* 129 (2) (1996) 263–283 (1996).
- [30] K. Salari, P. Knupp, *Code verification by the method of manufactured solutions*, Tech. rep., Sandia National Labs., Albuquerque, NM (US) (2000).
- [31] T. H. Pulliam, D. Chaussee, A diagonal form of an implicit approximate-factorization algorithm, *Journal of Computational Physics* 39 (2) (1981) 347–363 (1981).
- [32] J. W. Kim, D. J. Lee, Generalized characteristic boundary conditions for computational aeroacoustics, part 2, *AIAA Journal* 42 (1) (2004) 47–55 (2004).
- [33] E. Albin, Y. d’Angelo, L. Vervisch, Flow streamline based navier–stokes characteristic boundary conditions: modeling for transverse and corner outflows, *Computers & Fluids* 51 (1) (2011) 115–126 (2011).
- [34] C. K. Tam, F. Q. Hu, An optimized multi-dimensional interpolation scheme for computational aeroacoustics applications using overset grids, *AIAA Paper* 2812 (2004) 2004 (2004).
- [35] T. J. Poinso, S. Lele, Boundary conditions for direct simulations of compressible viscous flows, *Journal of Computational Physics* 101 (1) (1992) 104–129 (1992).
- [36] C. K. Tam, J. Hardin, *Second computational aeroacoustics (CAA) workshop on benchmark problems*, NASA CP-3352 (1997) (1997).